Hot Pressing and Characterization of Powder Based Silicon Substrates for Photovoltaic Applications.

Phillip Juven

Declaration

I declare that this work has been performed independently and in accordance with the rules and regulations for examinations at the Norwegian University of Science and Technology, NTNU

Phillip Juven

Trondheim, 10th of July 2012

Preface

This report has been written and conducted at the Department of Materials Science and Engineering at the Norwegian University of Science and Technology (NTNU) during spring 2012.

Numerous people have helped me with the experimental work. They all deserve my gratitude and are highly appreciated.

First of all I would like to thank my supervisor Adjunct Associate Professor Eivind Øvrelid at SINTEF Materials and Chemistry for his contribution to this master thesis and for his enthusiasm and engagement to the task. I would also like to thank the PhD-student Guttorm Syvertsen for training and guidance with the hot-press apparatus.

Last I would like to thank Senior Scientist Alexander Ulyashin for providing me with silicon powder.

Abstract

High purity silicon material in solar cell fabrication constitutes 40% of the total cost for conventional solar cell production. One approach to reduce costs would be to use less of this expensive silicon by making thin film solar cells and use a cheaper substrate as mechanical carrier.

In this work the main objective has been to manufacture silicon substrates from powder by hot-pressing. The effect of the sintering parameters has been characterized. A secondary objective was to look at the possibility to achieve larger grains by recrystallization.

Samples processed by hot-pressing silicon powder of metallurgical grade with varying temperatures (1200-1375 °C), pressures (30-50 MPa) and sintering time (30-60 min) has been carried out. Halogen lamps were used for heat treatment for specific samples after hot-pressing. Microstructure and porosity were characterized using optical and electronic microscopy. EBSD was used to determine the grain size and grain orientation. The density was determined by Archimedes' method. Resistivity was measured by a conductive probe.

Densities higher than 90 % were obtained at high temperatures and pressures. The time conducted at maximum temperature during hot-pressing was not of vital importance with respect to density.

The mean particle size of the powder was determined to ~20 μm, while hot-pressed samples had an average grain size of ~30 μm. The samples showed low resistivity due to high impurities of the silicon powder. High surface porosity was found for the less dense samples. Recrystallization was successfully achieved for the sample hot-pressed at 1350 °C, 30 MPa and 30 min, resulting in elimination of pores and significant grain growth from 31,83 to 56,96 μm.

Characterizations of the hot-pressed samples are limited to the methods and techniques described above.

Sammendrag

Høy superrent silisium i solcellefabrikasjon utgjør 40% av de totale kostnadene for konvensjonell solcelleproduksjon. En mulighet for å redusere kostnadene er å bruke mindre av dette dyre materialet ved å lage tynnfilm solceller basert på et billig substrat som mekanisk bærer.

I dette arbeidet har hovedmålet vært å produsere silisiumsubstrat ved å varmpresse silisiumpulver. Effekt av sintringsparametre har blitt karakterisert. Et sekundært mål var å se om det var mulig å oppnå større korn ved rekrystallisering.

Prøver av silisiumpulver av metallurgisk grad har blitt varmpresset med varierende temperatur (1200-1375 °C), trykk (30-50 MPa) og sintringstid (30-60 min). Halogenlamper ble brukt for varmebehandling av spesifikke prøver etter varmpressing. Mikrostruktur og porøsitet ble karakterisert vha lys- og elektronmikroskop. EBSD ble brukt til å bestemme kornstørrelse og kornorientering. Tettheten ble bestemt av Archimedes' metode. Resistivitet ble målt av en målesonde.

Tetthet høyere en 90% ble oppnådd ved høy temperatur og trykk. Sintringstid ved maksimal temperatur under varmpressing var ikke av avgjørende betydning med hensyn på tetthet.

Gjennomsnittlig partikkelstørrelse av pulveret ble bestemt til ~20 μm, mens de varmpressede prøvene hadde en gjennomsnittlig kornstørrelse på ~30 μm. Prøvene viste lav resistivitet pga høye forurensninger i pulveret. Prøver med lav tetthet hadde høy overflateporøsitet. Rekrystallisering ble oppnådd for prøven produsert ved 1350 °C, 30 MPa og 30 minutter, som resulterte i eliminering av porer og betydelig kornvekst fra 31,83 til 56,96 μm.

Karakterisering av de varmpressede prøvene er begrenset til de metoder og teknikker som er nevnt ovenfor

.

Table of Contents

List of Acronyms

Ar	Argon
BN	Boron nitride
CSiTF	Crystalline silicon thin-film
CVD	Chemical Vapor Deposition
EBSD	Electron Backscatter Diffraction
He	Helium
IPF	Inverse Pole Figure
MG-Si	Metallurgical Grade Silicon
N_2	Nitrogen gas
SEM	Scanning Electron Microscope
SiO_2	Silicon dioxide
SiO	Silicon oxide
SiC	Silicon carbide
SG-Si	Solar Grade Silicon
ZMR	Zone Melting Recrystallization

Sample Abbreviations

1200/50/30	Sample hot-pressed at 1200 °C, 50 MPa and 30 minutes
1300/50/30	Sample hot-pressed at 1300 °C, 50 MPa and 30 minutes
1325/50/30	Sample hot-pressed at 1325 °C, 50 MPa and 30 minutes
1350/50/30	Sample hot-pressed at 1350 °C, 50 MPa and 30 minutes
1375/50/30	Sample hot-pressed at 1375 °C, 50 MPa and 30 minutes
1300/30/30	Sample hot-pressed at 1300 °C, 30 MPa and 30 minutes
1325/30/30	Sample hot-pressed at 1325 °C, 30 MPa and 30 minutes
1350/30/30	Sample hot-pressed at 1350 °C, 30 MPa and 30 minutes
1300/30/60	Sample hot-pressed at 1300 °C, 30 MPa and 60 minutes
1325/30/60	Sample hot-pressed at 1325 °C, 30 MPa and 60 minutes
1350/30/60	Sample hot-pressed at 1350 °C, 30 MPa and 60 minutes
1300/50/60	Sample hot-pressed at 1300 °C, 50 MPa and 60 minutes
1325/50/60	Sample hot-pressed at 1325 °C, 50 MPa and 60 minutes
1350/50/60	Sample hot-pressed at 1350 °C, 50 MPa and 60 minutes

1 Introduction

High purity silicon material in solar cell fabrication constitutes 40% of the total cost for conventional solar cells productions [1-3]. Hence a major motivator for solar cell research and development is therefore a reduction in cost of the finished module. One approach to reduce costs would be to use less of this expensive silicon by making thin film solar cells and use a cheaper substrate as mechanical carrier [1, 3, 4].

A proposal is to deposit a layer of solar-grade silicon onto a low cost substrate of metallurgical grade silicon (MG-Si) [2]. The substrate is processed by hot-pressing of silicon powder. This will avoid the silicon waste from wire sawing kerf loss, which is typically 150-200 μm thick for each wafer [3]. Due to the impurities of MG-Si, the substrate is conductive and can be used as electrode, and it will provide good crystallization conditions for any silicon based layers deposited and annealed at appropriate conditions [2].

In this work the main objective has been to manufacture silicon substrates from powder by hot-pressing. MG-Si powder has been hot-pressed at varying temperatures, applied pressures and time. The Si substrates have been characterized with respect to density, microstructure, porosity, resistivity and grain orientation.

1.1 Motivation for Using Silicon Substrate as Mechanical Carrier for Thin-Film Solar Cells

Thin-film technologies have the potential for substantial cost advantage versus traditional wafer-based crystalline silicon due to lower material use (typically 100x less), fewer processing steps, and simpler device processing and manufacturing technology for large modules and arrays [5, 6].

Today, wafer-based crystalline silicon cells dominate the PV module market where 40 % of the silicon module costs is from the silicon wafers [2]. In addition, there is a steadily growing global production volume of Si solar modules that brings about a shortage in Si supply. Hence there is necessary to use thinner Si wafers in order to save Si material [7]. Thereby the driving force for thin film technologies has been, in part, driven by material costs and shortage of Si feedstock [2, 6, 7]. A solution for cost reduction is to use less of the expensive silicon by making thin Si-films on a low purity and cheap Si substrate as mechanical carrier [2, 3].

ThinSi is developing a crystalline silicon thin-film (CSiTF) solar cell that is based on a low cost MG-Si substrate with a high quality and pure active Si layer deposited on the surface. The low purity of the Si substrate is of metallurgical grade, which is highly conductive due to high concentrations of impurities. In addition, metallurgical Si powder costs less than $5/kg and will therefore significantly reduce the overall costs of the cell. The Si-substrates could be processed by conventional methods for production of Si wafers, i.e. by casting steps followed by cutting into ingots and sawed to wafers, but such conventional processing of Si wafers can be substituted by cost-effective powder-to-wafer processing using ceramics technology, thus avoiding costly wafering steps. This is done by hot pressing Si-powder into substrates, which lead to a perfect lattice match for the deposited thin film [2].

1.2 Concept of Crystalline Silicon Thin-Film with Silicon Substrate

CSiTF is made by depositing a thin layer of Si with a thickness of less than 50 μm onto a substrate. The substrate enhances the mechanical strength and avoids breakage of the thin film [7]. As for the wafer based solar cell the CSiTF solar cell has the

potential for high and stable efficiencies, is abundant and non-toxic, but requires only about 10% of the expensive high-purity silicon [8].There are two main approaches for deposition of the film; the low temperature substrate approach (LTS) and the high temperature substrate approach (HTS). LTS are deposited at temperatures up to 550°C, usually on glass substrates [7]. It is not applicable for Si-substrates and will therefore not be treated further in the present paper. For HTS, a high silicon deposition rate (using deposition rates up to 1300°C) can be reached, with the possibility to obtain large crystal grains by melt recrystallization. As these substrates are of silicon, their behavior at high temperatures is matching the deposition/crystallization processes of thin Si layer on top [2, 7, 8].

M. Grau et. al [3] made crystalline silicon thin-film with silicon substrate. The hot-pressed silicon bed was covered on one face by an intermediate layer of silicon oxide. p^+ doped silicon was then deposited by chemical vapor deposition (CVD) on the intermediate layer. The layer was used as a seeding layer for the growth of the active silicon layer, but as deposited it was not crystalline. Therefore zone melting recrystallization (ZMR) was applied, which allowed the obtaining of the multicrystalline silicon as a seeding for the rest of the wafer. As the SiO_2 layer is electrically insulting, a part of the layer needed to be removed to allow carrier collection. This was done with laser fired rear access, which is a punctual laser ablation of the intermediate layer and seeding layer. At last the absorbing p-type Si layer was epitaxial deposited by CVD on the seeding layer.

Figure 1 shows a schematic of the solar cell structure based on a low-cost Si substrate. The structure is very similar to conventional bulk crystalline Si solar cells, except from that the substrate substitutes the Si wafer [2].
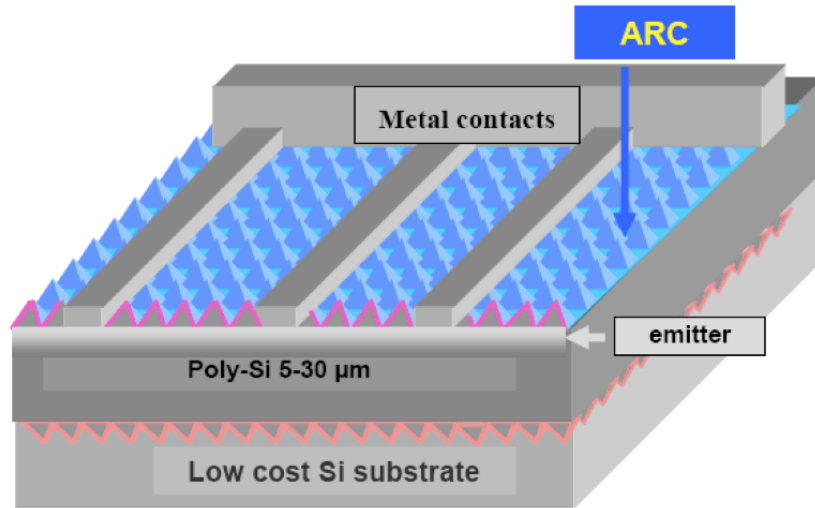
Figure 1 General structure of solar cell based on low-cost Si substrate [2].

2 Theory

2.1 Hot-Pressing (HP)

Hot-pressing, also referred to as pressure sintering or pressure-assisted sintering, is a method for the densification of metallic or ceramic material by putting powder into a die and applying force with uniaxial pressure heads [9]. A hot-press consists of a furnace surrounding a high-temperature die with a press in-line to apply a controlled load through the die pistons, see Figure 2. The application of pressure at the sintering temperature accelerates the kinetics of densification by increasing the contact stress [10, 11]. The early stage is dominated by particle rearrangement and plastic flow, and at the late stage grain boundary and volume diffusion become controlling [9, 12]. Atoms diffuse to points of contact, creating bridges and reducing the pore size [13].
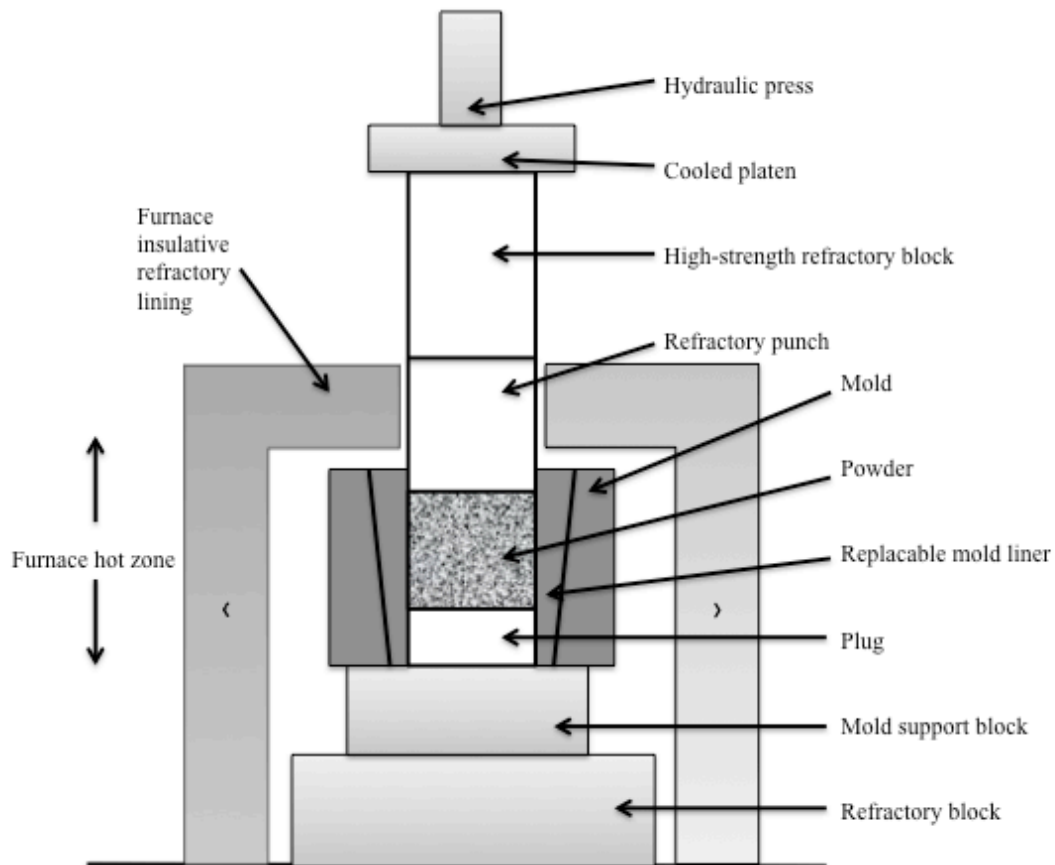

Figure 2 Schematic showing the essential elements of a hot uniaxial pressing.

The primary driving force for densification of a compact powder at high temperatures is the change in surface free energy. Small particles have high surface free energy and thus have a strong thermodynamically drive to decrease their surface area and bond together. Typically, the finer the powder, the greater the surface area and lower temperature, pressure and time is needed for densification [10].

Induction heating, with water-cooled coils is most commonly used. The furnace must either be evacuated or backfilled with Ar, N_2, or He during operation to minimize oxidation of the graphite [10].

The die material must withstand the temperature, transient thermal stresses, high hot-pressing loads and be chemically inert to the material being hot pressed. Graphite is the most often used die and piston material. It has a high temperature capability, high strength and low coefficient of friction.

The source of pressure is usually a hydraulic press with a water-cooled platen attached to the pressing ram. However, this does not provide adequate cooling to extend the ram into the furnace, so blocks of graphite are commonly used.

Reactivity is a special concern of die assemblies so graphite dies are often spray coated with BN to prevent sticking [10].

Hot-pressing permits achieving near theoretical density and very fine grain structure, which result in optimization of strength. External pressure speeds up the process of compacting and reduces its temperature. As a result, samples obtained are of high density close to 100% theoretical density. The applied stress minimizes porosity and grain growth, which results in higher strength than for sintering. Also it can be conducted starting with a loose powder where no binders or other organic additives are required [10, 14].

Compressed powder has a concentrated stress in the contact region. In pressures-assisted sintering, low stresses (less than 0,5 MPa) enhance sintering due to stress concentration. The external pressure is amplified in the microstructure. This amplified pressure is termed the effective pressure, and depending on the microstructure it can be several times higher than the applied pressure.

Stress is the force over the contact area, so for fixed loading the effective stress depends on the size of the particle contacts. If the contacts between the particles are small, the effective stress at the contacts is high. As the contacts grow the stress diminishes.

During hot-pressing the applied pressure is often constant and effective pressure or stress at the particle contacts falls continuously with densification. The effective pressure determines the mechanism and rate of sintering enhancement.

The effective pressure is larger than the applied pressure since the pores cannot carry stress [15, 16]. At the first stage in pressure sintering the particles rearrange. The pressure is concentrated at the small initial particle contacts. It is very high and the number of contacts and the contact size influence the densification rate due to an external pressure. During densification the contacts grow and new contacts form as the particles centers approach one another [17]. The new contacts carry a fraction of the applied pressure and thereby reduce the effective pressure. Further, grain boundaries contribute a surface energy, and the replacement of pores with the extension of grain boundary area further reduces the effective sintering stress [18].

For powders with a wide particle size distribution, the initial packing density is high. The densification is fast due to more contacts and higher effective pressure compared to monosized particles. For uniaxial hot-pressing, the contacts aligned with the pressing direction are larger by a factor of 2 over the contacts perpendicular to the pressing direction. This results in anisotropic densification.

Gas entrapped inside pores limits the final density. If the grains are small with respect to the final pore size, the closure of pores is not favorable. For large grains with respect to pores, pressure is useful in elimination of the pore, see Figure 3.
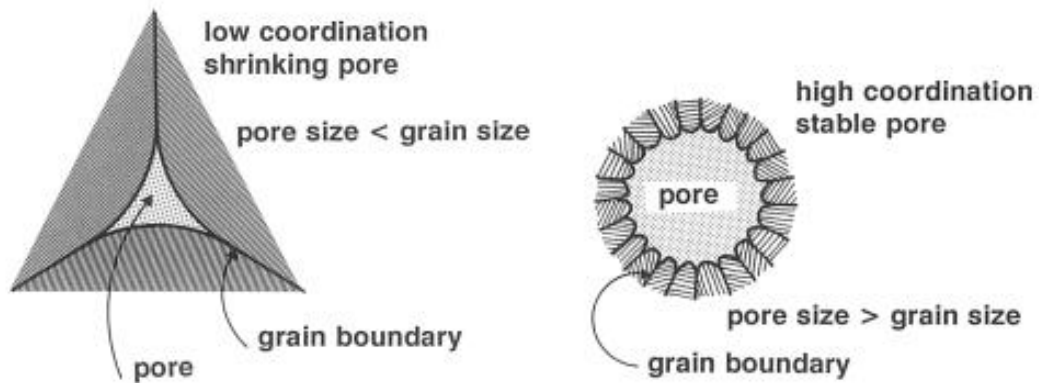
Figure 3 Possible extremes for the relative grain size and pore size [12].

The mechanical properties of a material is affected by the temperature. For most materials the strength decreases at high temperatures. With pressure applied into the system the densification is caused by plastic flow. This plastic flow is determined by the effective stress at the particle contacts, which is related to the material yield strength at the consolidation temperature. Figure 4 illustrates the important densification role of pressure using constant-stress hot pressing data for both copper and magnesia. The density at zero time goes up with applied pressure, reflecting the important initial role of plastic flow. Note the characteristic behavior of a decreasing rate of densification as density and time increase [12].
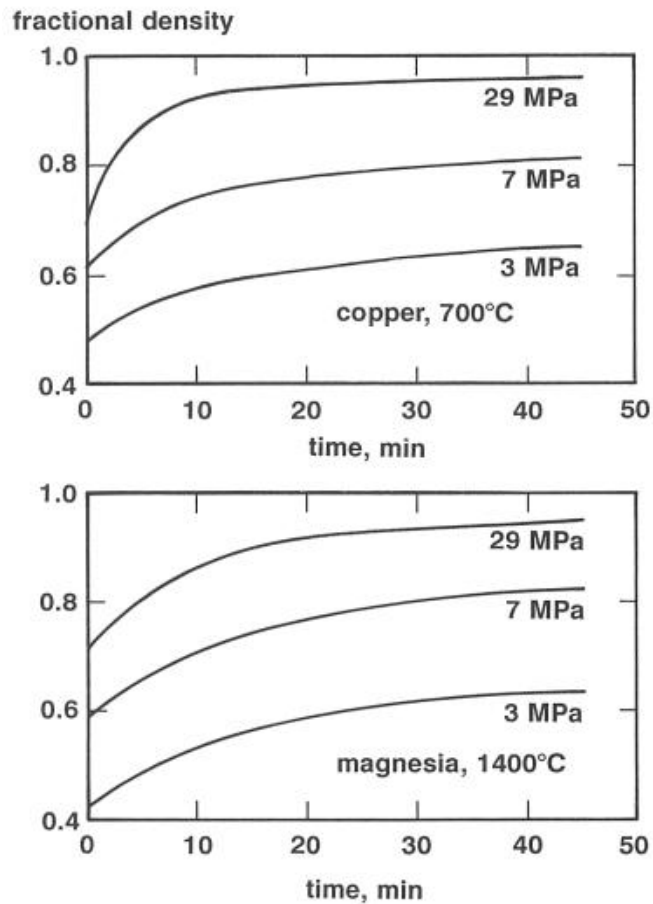
Figure 4 Plot of density versus time showing the dependence of pressure for metallic and ceramic materials, and the decreasing rate of densification with increasing time [12].

Pressure sintering of a crystalline material typically involves the combined motion of point defects and dislocations. Faster densification by creep processes requires higher temperatures and stresses. Atomic motions depend on the temperature. Higher temperature improves densification when creep controls mass flow [12]. This is illustrated in Figure 5.
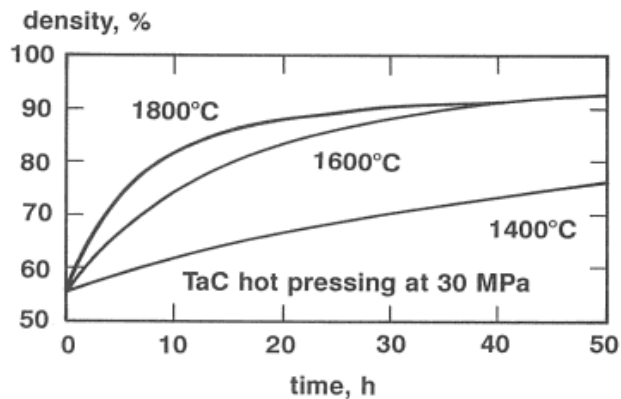
Figure 5 Temperature effect on hot-pressing for tantalum carbide subjected to 30 MPa pressure [12].

A problem with hot-pressing is to achieve uniform density throughout the pellet being pressed. This is due to a combination of loose powder loading and nonuniform temperature distribution. If the loose powder has very low thermal conductivity, the edges in close proximity to the graphite are heated up faster than the interior and begin to sinter. This physically shifts material from the center toward the edge and ultimately results in the density and strength gradient. The problem can be resolved by precompacting the powder better and by modifying the time and temperature profile during hot-pressing [10].

Another concern, is that the die is essentially closed, so the atmosphere in the die can be inferior to that in the furnace chamber [12].

Friction with the die walls that cause shear stresses that can lead to cracking. This shear stress is roughly proportional to the applied stress, leading to the concept of an effective Poissons′s ratio [12].

There is no theoretical limit for the size of the substrate. The thickness is determined by the amount of powder used during hot-pressing [3]. A. Derbouz Draoua et. al [19] produced 50 – 90 mm diameter silicon wafers with thicknesses between 300 and 600 μm by pressure sintering at temperatures up to 1350 °C. The powder was introduced into dies of different forms and pressed in the range of 7-35 MPa.

2.2 Archimedes' Principle

Archimedes principle can be used to measure the bulk density of any shape. It states that a body of any shape partially or completely submerged in a fluid is buoyed up by a force equal to the weight of the fluid displaced by the body [11]. Numerous variations of the Archimedes principle exist for different purposes. According to ISO 5017:1998 [20], one method for determining the density is by first measuring the dry weight of the sample (m_1), followed by weighing the sample suspended in isopropanol (m_2) and then weigh the sample in air (m_3). The bulk density, apparent porosity and true porosity of the sample can then be calculated:

Bulk density ρ_b, expressed in grams per cubic centimeter, is given by the equation

$$\rho_b = \frac{m_1}{m_3 - m_2} \times \rho_{liq} \qquad (2.1)$$

Apparent (open) porosity π_a, expressed as a percentage by volume, is given by the equation

$$\pi_a = \frac{m_3 - m_1}{m_3 - m_2} \times 100 \qquad (2.2)$$

True porosity π_t, expressed as a percentage by volume, is given by the equation

$$\pi_t = \frac{\rho_t - \rho_b}{\rho_t} \times 100 \qquad (2.3)$$

Theoretical density is given by the equation

$$\rho_t = \frac{m}{V} = \frac{\frac{Z \times M}{N_A}}{a \times b \times c} \qquad (2.4)$$

where m is the mass in g, V is the volume in cm^3, Z is the number of atoms pr. unit cell, M is the molar mass, N_A is Avogadro´s number and a,b,c are lattice parameters.

2.3   Basic Resistivity and Conductivity Theory

Electrical conductivity in a solid is attributable to electrons that are free to move under the influence of an applied electric field [21].

Resistivity is a measure of how strongly a material opposes the flow of an electric current. An electric field inside a material will cause electric current to flow. The resistivity (ρ) is defined as:

$$\rho = \frac{E}{J} \qquad (2.5)$$

where ρ is the resistivity given in Ωm, E is the magnitude of the electric field in Vm^{-1} and J is the magnitude of the current density in Am^{-2}.

Conductivity (σ) in a solid is attributable to electrons that are free to move under the influence of an applied field. It is the inverse of resistivity.

$$\sigma = \frac{1}{\rho} \qquad (2.6)$$

where σ is measured in Sm^{-1}.

2.3.1 Resistivity as function of doping level
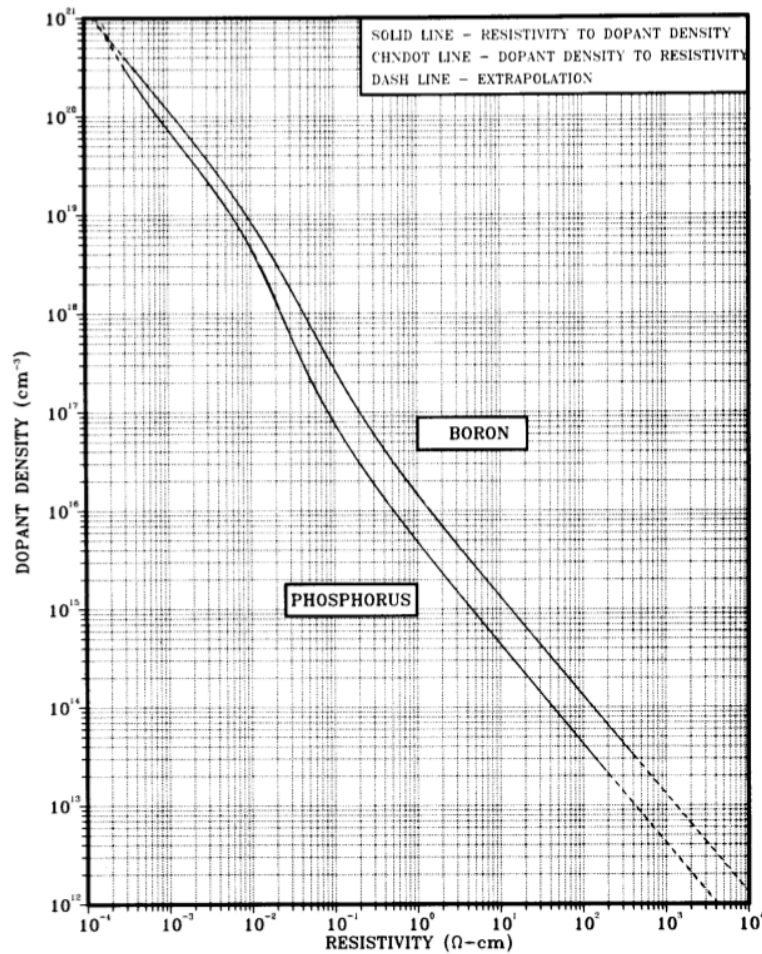
Figure 6 Conversion between resistivity and total dopant density values for boron- and phosphorus-doped silicon [22].

Impurity atoms can be incorporated either by interstitial impurities where they can occupy positions squeezed in between the atoms of the host crystal, or by substitutional impurities where they can substitute an atom of the host crystal. Atoms from group III and V in the periodic table acts as substitutional impurities in silicon.

A group III impurity (e.g B and Al) have not enough valence electrons to satisfy the four covalent bond. This gives rise to a hole tied to the group atom [23]. Figure 6 illustrates conversion between dopant density and resistivity for boron- and phosphorus-doped single crystal silicon. The data can be extended to other dopants in silicon that have similar activation energies [22].

2.4   Recrystallization of Silicon by Zone Melting Recrystallization

Recrystallization can be achieved by thermal treatment to the sample in order to get a complete densification. In this process deformed grains are replaced by a new set of undeformed grains into new, equiaxed, and dislocation-free grains. The recrystallization temperature is not a fixed temperature, like melting temperature for pure elements [13].

Bellanger et. al [24] recrystallized pressure sintered micro sized solar grade silicon (99,9999% purity) with two halogen lamps of 1000W. The sample was kept vertically thanks to an adequate support, and on both sides, two elliptic mirrors focused the radiation from the lamps. The sample was then moved up and down at a speed of a few mm/min. The process was made under 1 l/min of argon flow. This procedure increased the size of the grains from some microns to some millimeters range. Also the recrystallization decreased the oxygen concentration where it was assumed that SiO_2 precipitates were dissolved and evaporated as SiO and O_2.

A. Draoua et. al [19] did a similar experiment where they produced pellets with 50 mm in diameter and thicknesses between 300 and 600 μm at 30 to 35 MPa. The powder consisted of agglomerates with the size-range of 5 to 10 μm. They also produced 90 mm samples with very uniform thickness between 200 and 250 μm. However these samples were less dense than 50 mm ones due to the 10 MPa limitation of the pressing tool. The ZMR was powered by high power linear halogen lamps. In the process, the hot pressed samples were partially recrystallized and the grain growth was controlled along the surface. After ZMR the grain size significantly increased from 3 to 100 μm, see Figure 7.
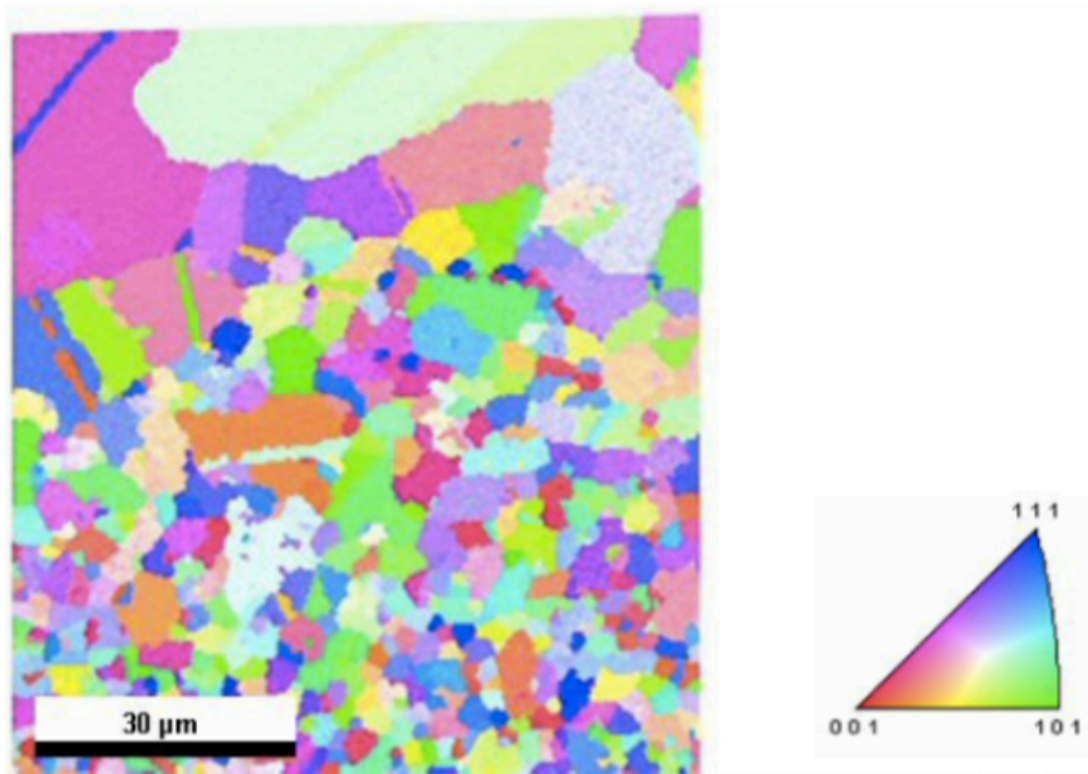
Figure 7 Electron backscatter diffraction (EBSD) image of hot pressed silicon sample after ZMR annealing. The top part of the images shows the recrystallized area whit significant grain growth [19].

2.5 Scanning Electron Microscopy

The scanning electron microscope (SEM) permits observation and characterization of organic and inorganic materials on nano or micrometer scale. It is a popular technique due to the high resolution and the depth of field obtained in the images. The area to be analyzed is swept by a finely focused electron beam, and the interaction between the electron beam and sample give rise to different signals picked up by the respective detectors [25].

The electron gun, normally a tungsten filament, emits electrons that are accelerated towards an anode. The potential difference between anode and cathode is in the interval 1-40 kV. The electrons travel through a column subjected to a vacuum. The column consists of tree magnetic lenses that focus the electron beam, an aperture to limit the beam divergence and a scanning coil. When the electron hits the sample secondary electrons, backscatter electrons, X-rays, Auger electrons or photons may be detected. Normal SEM images consist of signals from backscatter or secondary electrons. When a signal is detected, it is amplified and sent to a display unit. Since

14

the scanning of the display unit is synchronized with the electron probe scan, brightness variations depending on the number of electrons detected in that area appear on the monitor screen. These variations in intensity make up the SEM image [26].

2.5.1 Electron Backscattering Diffraction

Electron backscatter diffraction (EBSD) is microstructural crystallographic technique that can be attached to an SEM. It reveals grain size, grain boundaries, grain orientation, texture and phase identity of the sample under the beam [27].

At an operation, a flat and polished sample is put into the SEM chamber with a tilted angle of 70° from horizontal towards the diffraction camera. When the beam of electrons interacts with the crystal lattice in the sample, low energy backscatter electrons emerge from the sample. If a fluorescent phosphor screen is placed close to the sample, in the path of the diffracted electrons, an electron backscatter diffraction pattern (EBSP) can be seen, see Figure 8.
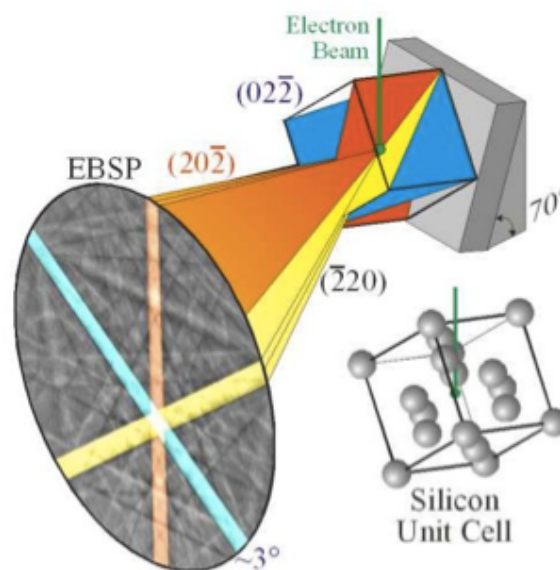
Figure 8 Electron interaction with crystalline material [28].

The symmetry and appearance of diffraction pattern is related to the crystal structure at the point where the beam interacts with the sample. By rotating the crystal, the orientation changes and so does the diffraction pattern [28].

Inverse pole figure (IPF) is used to show the positions and directions of individual grains. Each point in an IPF is colored according to an automatically color coded unit triangle of the IPF. For cubic phase materials, red, green and blue are assigned to the [001], [101] and [111] crystal orientation respectively [28], see Figure 9.
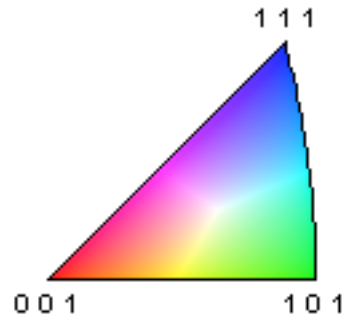
Figure 9 Inverse pole figure colored map.

3 Experimental Procedure

3.1 Powder characterization

The silicon powder was provided by Elkem and its composition is given in Appendix A. Laser diffraction using COULTER LS 230, was performed by Irene Bragstad at SINTEF.

3.2 The Hot-Press Process

The MG-Si powder, approximately 5,00 g, was introduced into a pure cylindrical shape of graphite surrounded by a high-strength graphite die.
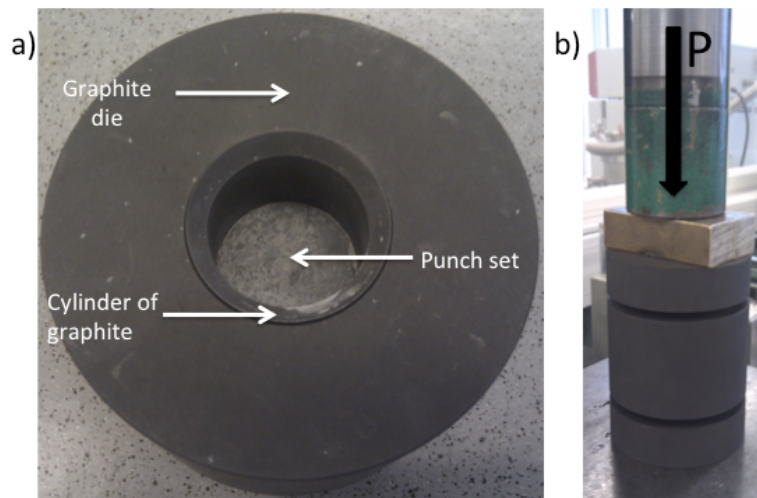
Figure 10 a) Parts of the die. b) Die was pre-pressed with applied load (P) similar to load under hot-pressing.

The punch set was spray coated with boron nitride in advance to isolate the powder from the graphite die and prevent possible interactions or sticking. Figure 10a, shows an image of the different components. The die was pre-pressed with a pressing tool, as shown in Figure 10b and Figure 11, to the maximum load to make sure that the system could handle the pressure.
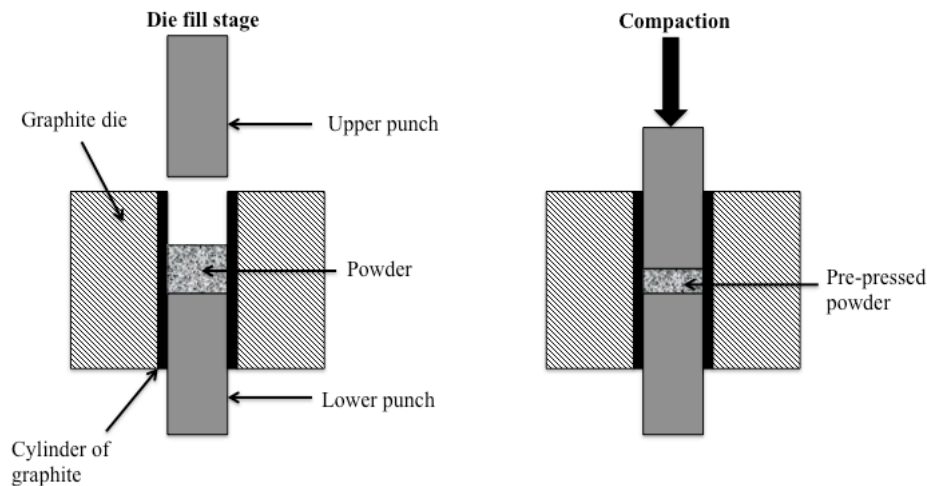
Figure 11 Cross section of the powder compaction

Hot-pressing was conducted by HP50-7010G. The furnace was lifted up to insert the die. The chamber was evacuated and refilled with flowing argon at atmospheric pressure during the experiments to avoid oxidation of carbon at high temperatures. Temperatures of 1200 – 1400 °C were used with heat rating of 10°C/min. When reaching the temperature, the load was applied for desired time from the bottom punch impacting the silicon powder.

After the sintering step the applied pressure was released followed by a cooling rate of 10°C/min. The cooling rate was lower than the configuration of the temperature controller, due to the fact that heat was not transported away from the components in the furnace quickly enough. This could be seen 2 hours after hot-pressing, when the temperature inside the furnace was at the range of 200-250 °C depending on time held at maximum temperature. This meant that the temperature of the pellet inside the graphite die was even higher since this was the heat source causing a cooling rate lower than 10°C/min. Figure 12 illustrate two examples for 30 and 60 minutes at 1300 °C of the simple pressure sintering steps. The graph is equal for higher temperatures, only the flattening is at a higher point on the y-axes.
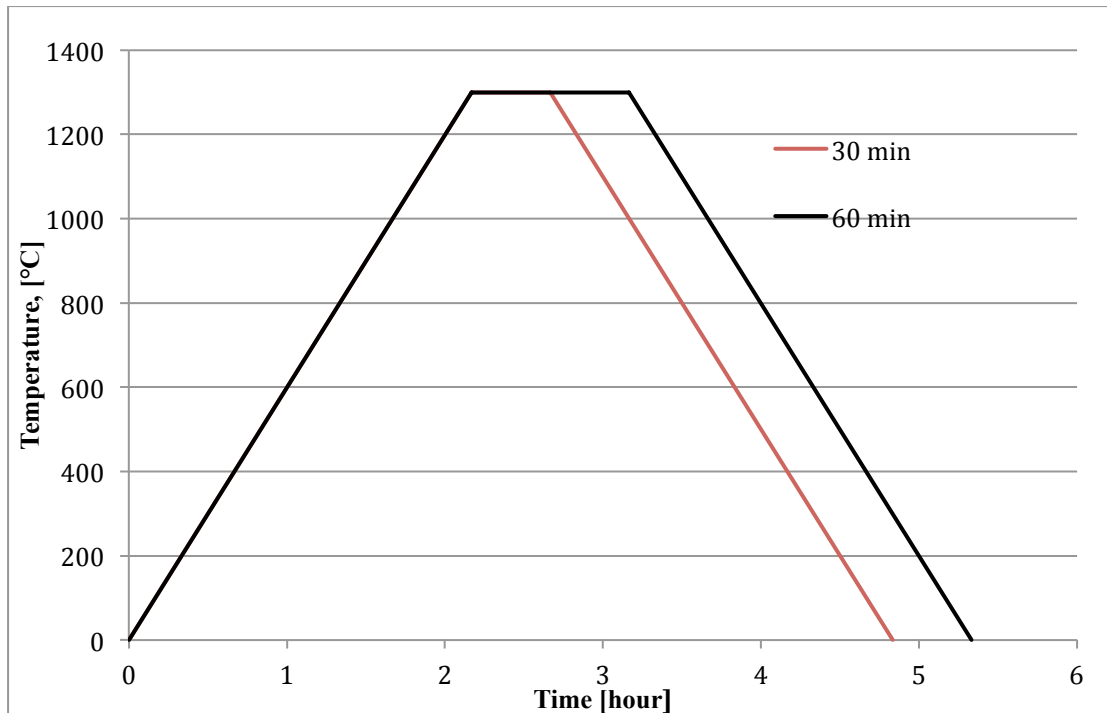
Figure 12 Temperature profile of the pressure sintered pellets at 30 and 60 minutes

The procedure was repeated for each sample, only varying the temperature, applied pressure and time.

In the present paper the samples are abbreviated as X/Y/Z, where X, Y and Z are the temperature (°C), applied pressure (MPa) and time (min) respectively. For example 1300/50/30 is the sample that has been conducted at 1300 °C, 50 MPa and 30 minutes. X/50/60, are samples that has been conducted at varying temperatures, but with constant pressure and time (50 MPa and 60 minutes). All the hot-press parameters for each pellet are given in Table 1. Notice that only one sample at 1375 °C was carried out.

Table 1 Hot-pressed parameters for all the pellets that were successfully conducted.

Sample nr	X (°C) / Y (MPa) / Z (min)
1	1200/50/30
2	1300/50/30
3	1325/50/30
4	1350/50/30
5	1375/50/30
6	1300/30/30
7	1325/30/30
8	1350/30/30
9	1300/30/60
10	1325/30/60
11	1350/30/60
12	1300/50/60
13	1325/50/60
14	1350/50/60

When the die was completely cooled down to room temperature, the pellet was pulled out with the same pressing tool used for pre-pressing by putting a cylindrical metal tool under the graphite die while applying force on the top side.

Some problem could occur when pulling out the sample, resulting in fracture. This is described in detail in chapter 5.3.

All the pellets were grinded on both surface sides before further characterization to eliminate BN from the punch sets that tended to stick on the surface.

3.3 Determination of Bulk Density, Apparent Porosity and True Porosity by Archimedes' Principle

Coarse grinding was performed on all samples before the densities were determined by Archimedes' Principle in accordance with ISO 5017. The following procedure is described for one specimen:

The sample was first weighed dry at atmospheric pressure (m_1). Then it was put in an air-tight vessel where the pressure was lowered to 13-15 mbar and held for at least 15 minutes in order to extract all of the air from open porosity of the sample. Next, the sample was immersed in isopropanol, while maintaining low pressure. After 30 minutes the vessel was filled slowly with air until it reached atmospheric pressure and it was kept like this for additional 30 minutes. Then the sample was weighed completely suspended in isopropanol (m_2). The temperature of isopropanol was noted

for the determination of the density of the liquid ($\rho_{isoprop}$). At last the sample was weight in air (m_3).

Archimedes' principle could be performed for several pellets at the same time, which made it less time consuming. Density and porosity calculations were done according to equation 2.1-2.4 in chapter 2.2.

3.4 Measuring Conductivity and Resistivity

Conductivity was measured in accordance with SIGMATEST 2.069, which is a battery operated portable instrument that measures the electrical conductivity of non-ferromagnetic metals based on the complex impedance of the measuring probe. The measuring range for the instrument is established by calibration. When unknown test pieces are measured the instrument converts the complex impedance value to an electrical conductivity value. During experiment, data at the center and at the edge of the pellet were measured. A sketch of the instrument is shown in Figure 13.
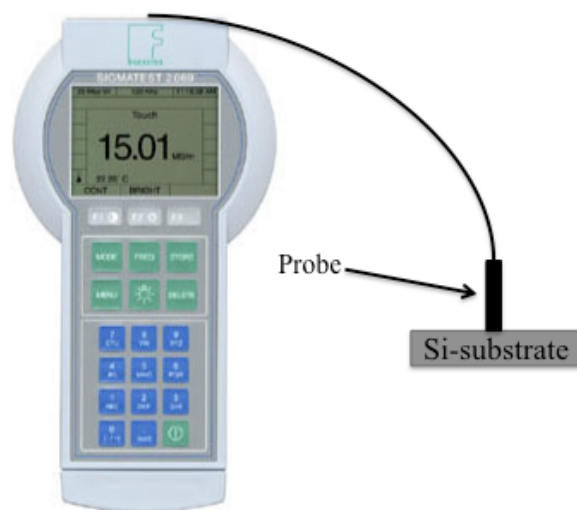
Figure 13 SIGMATEST 2.069 were used for resistivity measurements.

3.5 Sample preparation

Each sample was cut by a cutting tool. The circular blade was constructed with diamond segments, resulting in a relative smooth and fast (~20 sec) cutting.

1 piece from every pellet was prepared on the cross section side for characterization in optical microscopy and SEM. The pieces were prepared by cutting, mounting, grinding and polishing (see Figure 14a-d). Mounting with epoxy mixture (consisting

of resin and hardener) was required for easy grinding, due to the fact that the surface area was small and to obtain surface flatness. Then the samples were grinded on silicon carbide (SiC) abrasive paper to remove surface irregularities and damage introduced during cutting [11, 29], followed by polishing with diamond pastes with particle size of 3 μm and 1 μm on soft cloths.
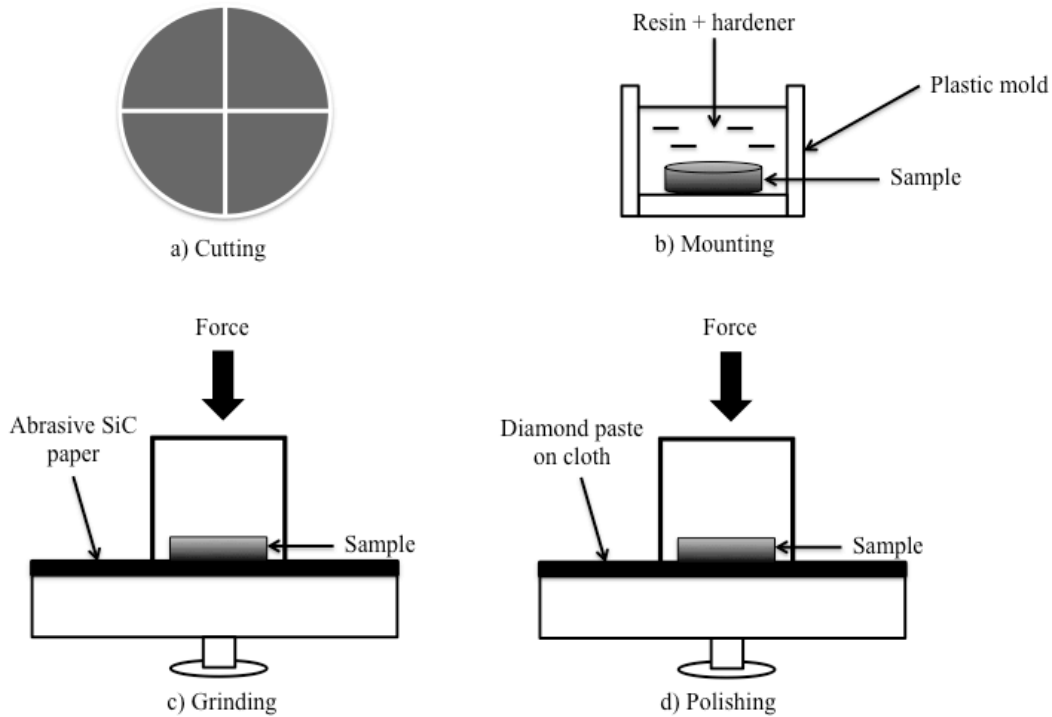
Figure 14 a - d. Sample preparations steps for optical microscopy and SEM.

3.6   Light Microscopy

The specimens were studied under the light microscope (Leica MEF4M) at 5X and 10X magnification to identify the porosity of the surface. The system was connected to a camera and a computer making it possible to take images by using the software ImageAccess easyLab 7.

The images taken at 10X magnification gave an overview of the surface, and images taken at 5X magnification were used to measure the porosity for each sample. The latter is described in detail in 3.6.1.

3.6.1   Surface Porosity

The surface porosity was measured by using the software ImageAccsess easylab. The following procedure is described for one sample: The inner part (meaning the surface

area close to the center of the pellet) and the outer part (meaning close to the outer edge of the pellet) was captured under 5X magnification, see Figure 15.
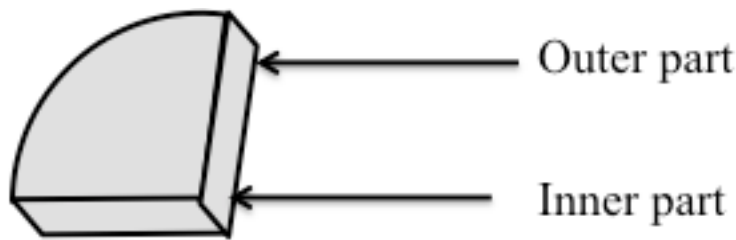
Figure 15 Images was taken at the inner and the outer part of the surface of the cross section polished area.

Then the image was analyzed in the software. By using "Particle analysis", the software could differ light (silicon) and dark (pores) areas. Sometimes the software neglected some areas of pores, which had to be added manually by clicking on the areas that were regarded as pores.

Knowing the calibration the software automatically figured out the area size of the image. An example is given Figure 16 for inner part of 1300/50/60 and 1350/50/60.

a) 1300/50/60 inner part   400 μm   b) 1300/50/60 inner part (porosity)   400 μm

c) 1350/50/60 inner part   400 μm   d) 1350/50/60 inner part (porosity)   400 μm
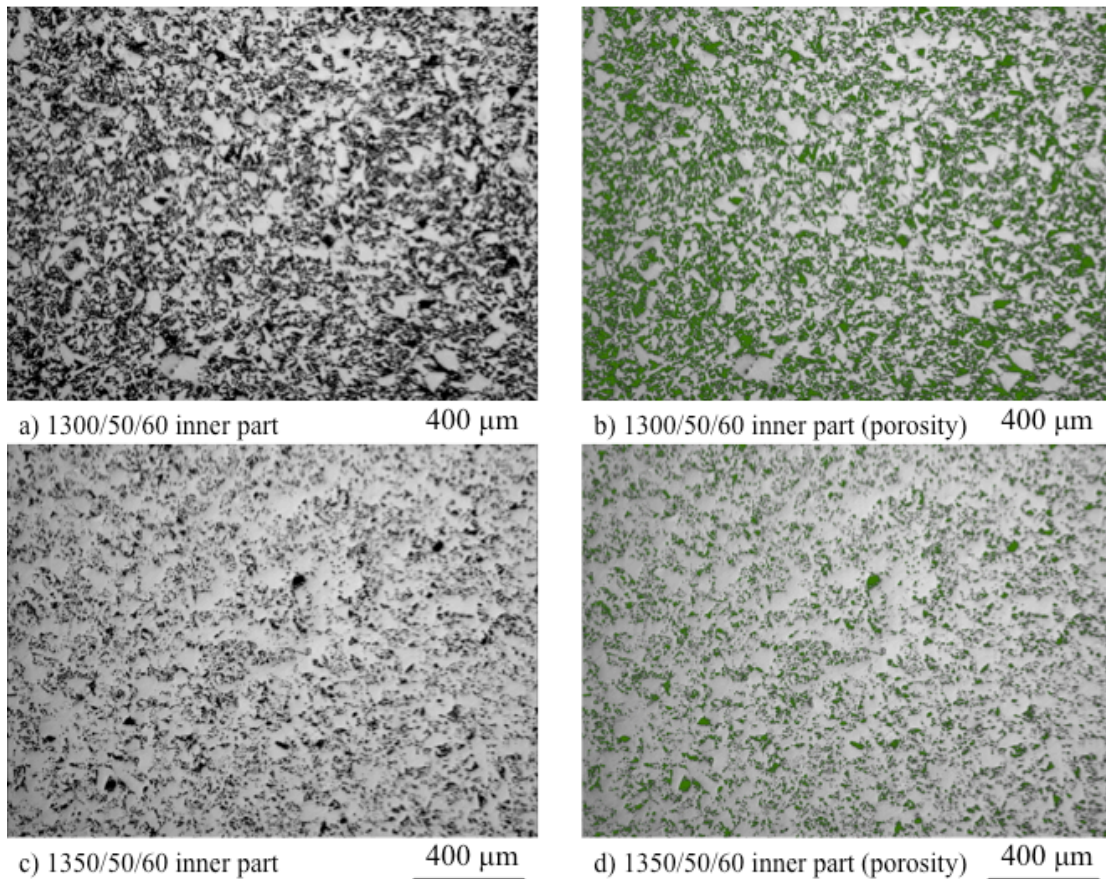
Figure 16 Particle analysis for 1300/50/60 and 1350/50/60.

All the images from the particle analysis are given in Appendix C.

3.7 Zone Melting Recrystallization by Halogen Lamps

Seven halogen lamps at 1000 W were used to try to recrystallize the samples. The lamps needed to be focused. This was done by turning on one lamp at the time and adjust the lamp so that the light illuminated on the area for recrystallization. By knowing the focal length for each lamp, a folding rule was used to measure the distance B (see Figure 17) to bring the rays in focus.
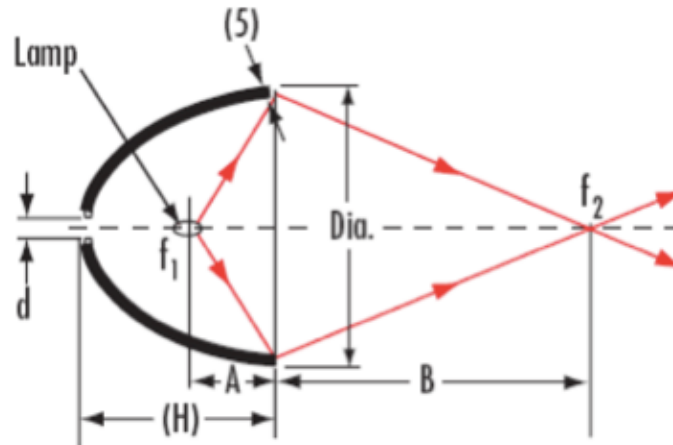
Figure 17 Cross section of halogen lamp showing the focus points f₁ and f₂ [30].

As mentioned in 2.4, earlier experiment of ZMR on silicon samples was done on substrates between 300 – 600 μm.

Micrometer thick pellets were not possible to achieve with the graphite dies used during hot-pressing. Therefore before ZMR, the samples were cut as thin as possible on the cross section side, followed by grinding to obtain surface flattening. By this ~2,5 mm thick samples were achieved.

Thin samples from 1300/30/30, 1325/30/30, 1350/30/30, 1350/50/30 and 1375/50/30 were illuminated by the halogen lamps for 4 minutes. After illumination, the samples were mounted, grinded and polished as described in chapter 3.5.

3.8 Electron Backscatter Diffraction

Zeiss Supra 55 VP LVFESEM was used for EBSD. The geometry configuration of the EBSD detector in this SEM was 20 mm as working distance with a tilting degree of 70°.

4 Results

4.1 Silicon powder

Figure 18 illustrates images obtained by SEM of the MG-Si powder. The particle size varies from few microns to ~100 μm and show irregular shape.
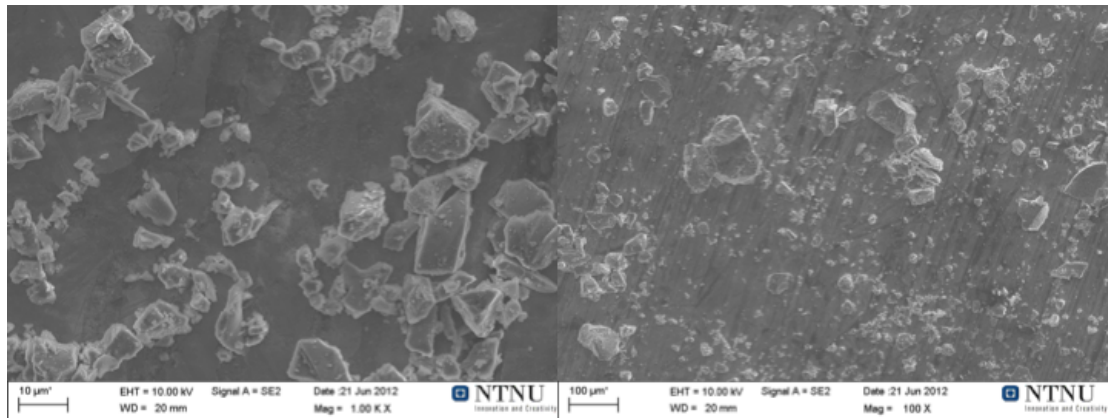
Figure 18 SEM pictures of the MG-Si powder at different magnifications.

The particle size distribution is given in Figure 19. The particle size varies from 0,4 μm to 105 μm. Mean particle size was determined to 20,36 μm. This is in accordance to the SEM images in Figure 18.
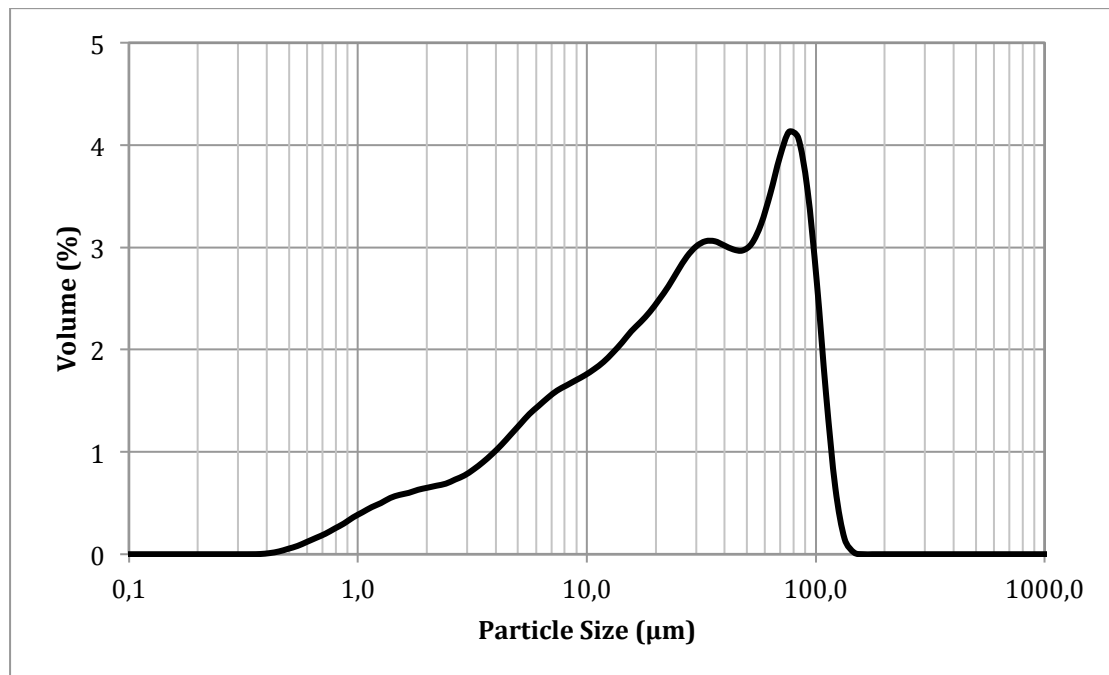
Figure 19 Particle size distribution of the MG-Si powder

4.2   Densification Behavior

Bulk density as a function of temperature for all the pellets are presented in Figure 20. As can be seen from the figure, the densities of the Si-pellets increase with increasing temperature. 1370/50/30 showed the highest density at 2,2393 g/cm^3. This is close to 100% theoretical densification of silicon, which is 2,3290 g/cm^3.
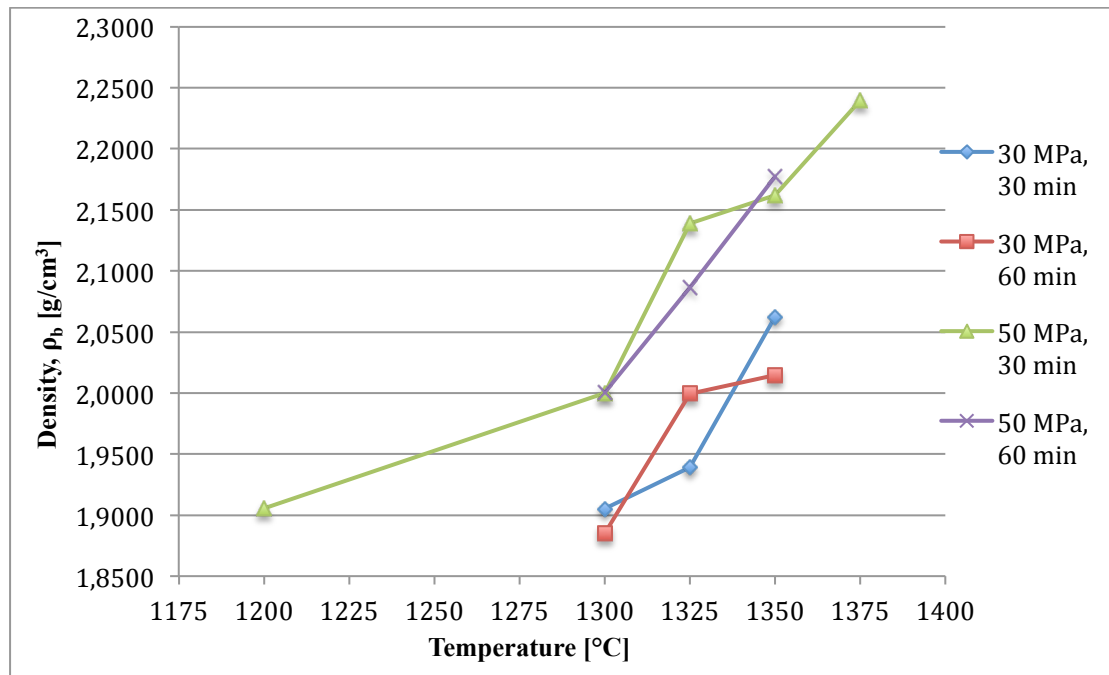
Figure 20 Bulk density of the silicon samples with respect to temperature.

Apparent and true porosity are shown in Figure 21 at varying temperatures.

As shown in Figure 21, the apparent and true porosity is decreasing with increasing temperature, because of the increase in density.

26
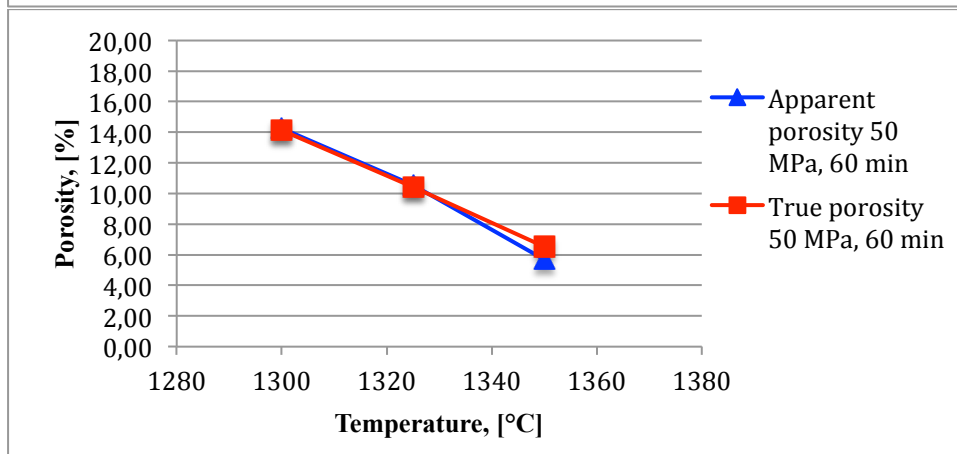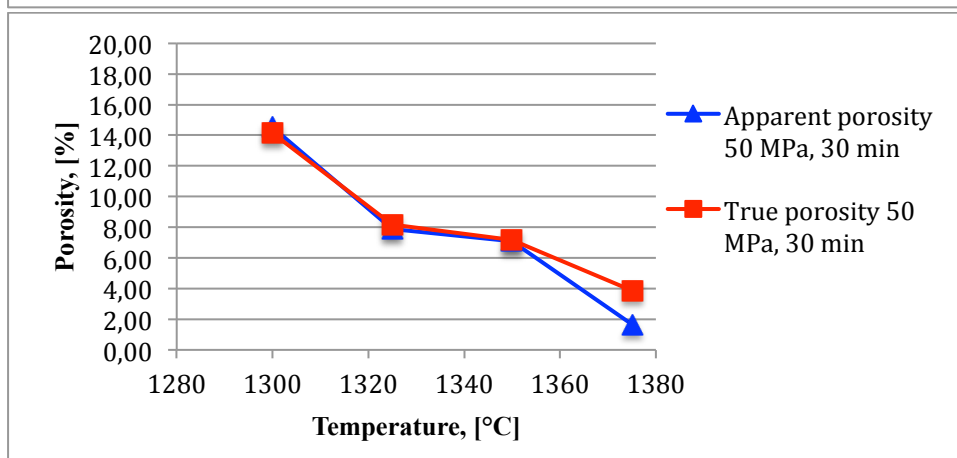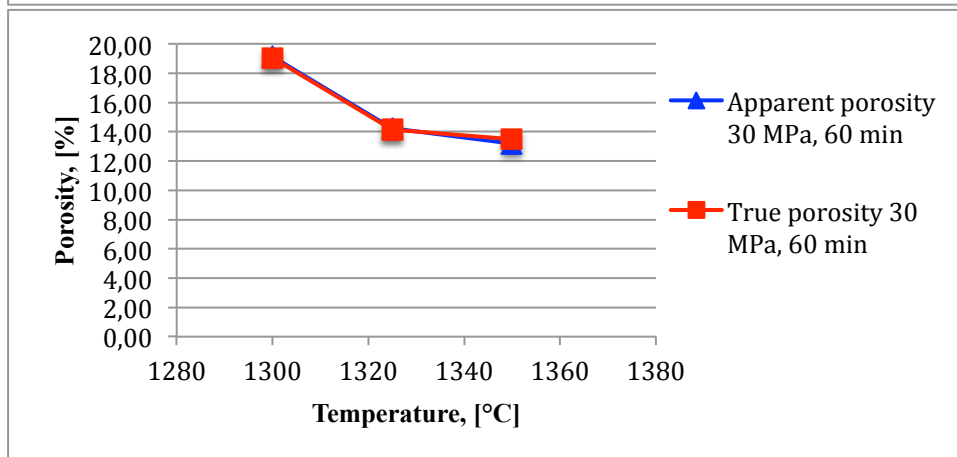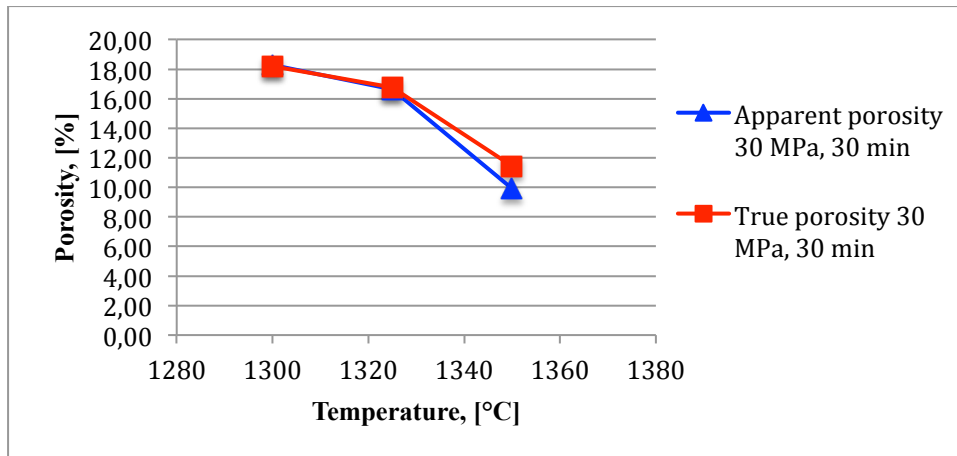
Figure 21 Apparent and true porosity versus temperature.

There are no significant difference in the values of the apparent and true porosity, meaning that the closed porosity is very small.

Data for determination of bulk density, apparent porosity, true porosity and density of isopropanol are given in Appendix B.

Figure 22 illustrates the improvement in densification due to the application of higher pressure. 50 MPa applied pressure resulted in higher densities than for 30 MPa at constant temperature.
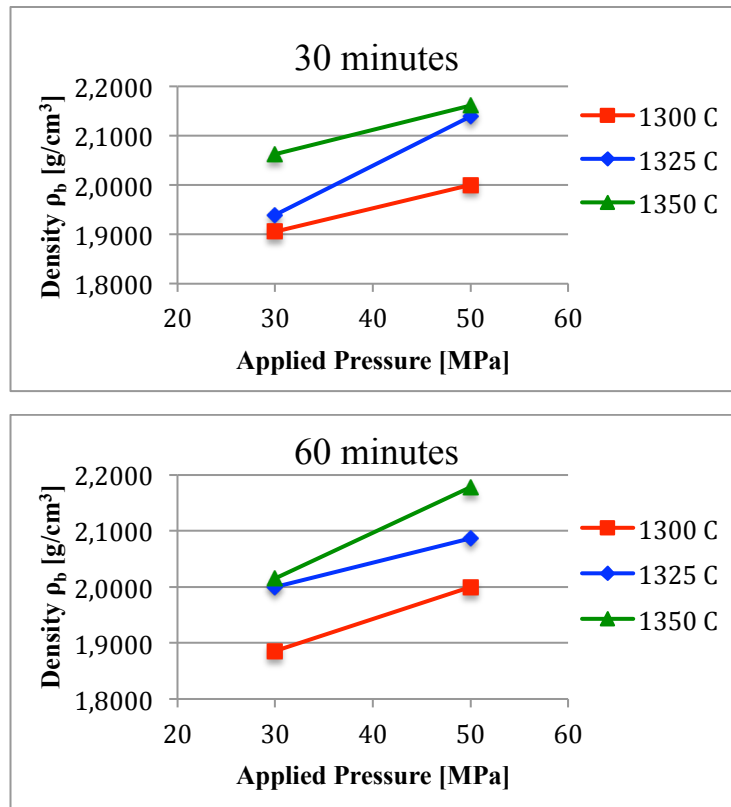
Figure 22 Density versus applied pressure for hot-pressing

Figure 23 illustrates the densification as function of time.

The initial role of plastic flow is obtained at a time < 30 min. The densification rate decreases with time, which is in accordance with Figure 4.
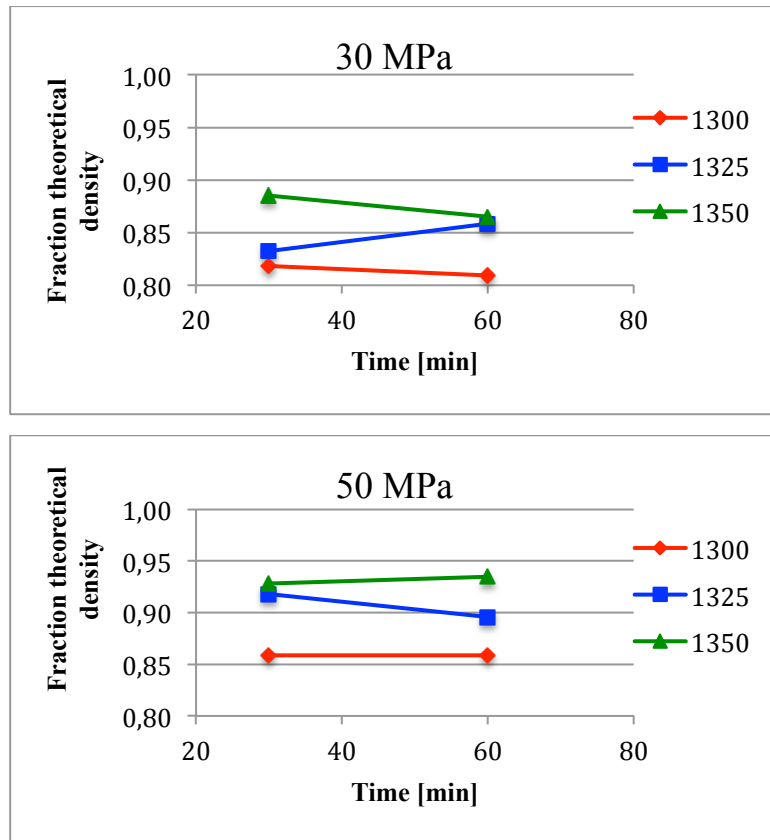
Figure 23 fractional densities versus time for hot-pressing

For some samples the density decreased with time. This is probably due to uncertainty in densification measurements and are discussed in 5.1.

4.3   Surface Characterization

4.3.1   Macro photo

Figure 24 shows a macroscopic image of a hot-pressed MG-Si pellet with 25 mm diameter and 5,5 mm thickness.
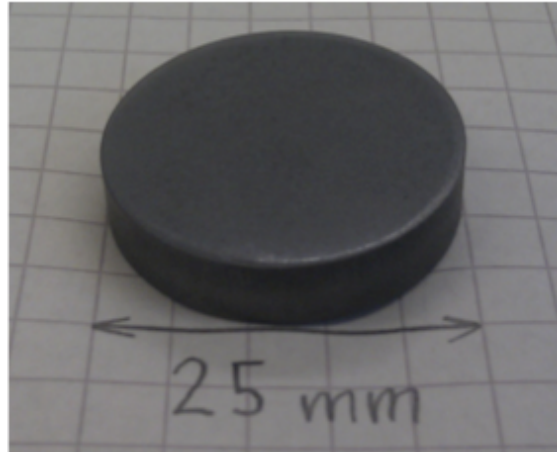
Figure 24 Macro photo of hot-pressed MG-Si

4.3.2   Light microscopy

The images obtained by light microscopy, Leica MEF4M, at 10X magnification are given in Figure 25– 27. From the Figures it is clear that the silicon (bright constituents) are packed denser at increasing temperatures. Also the pressure influences the packing. This can for example be seen by comparing 1) 1300/30/30 and 1300/50/30 and 2) 1350/30/60 and 1350/50/60. The pressure sintering time however does not play a major impact on the density based from the images illustrated below. This is also in accordance with density vs time curve in Figure 23.

a) 1300/30/30 100 µm

b) 1325/30/30 100 µm

c) 1350/30/30 100 µm
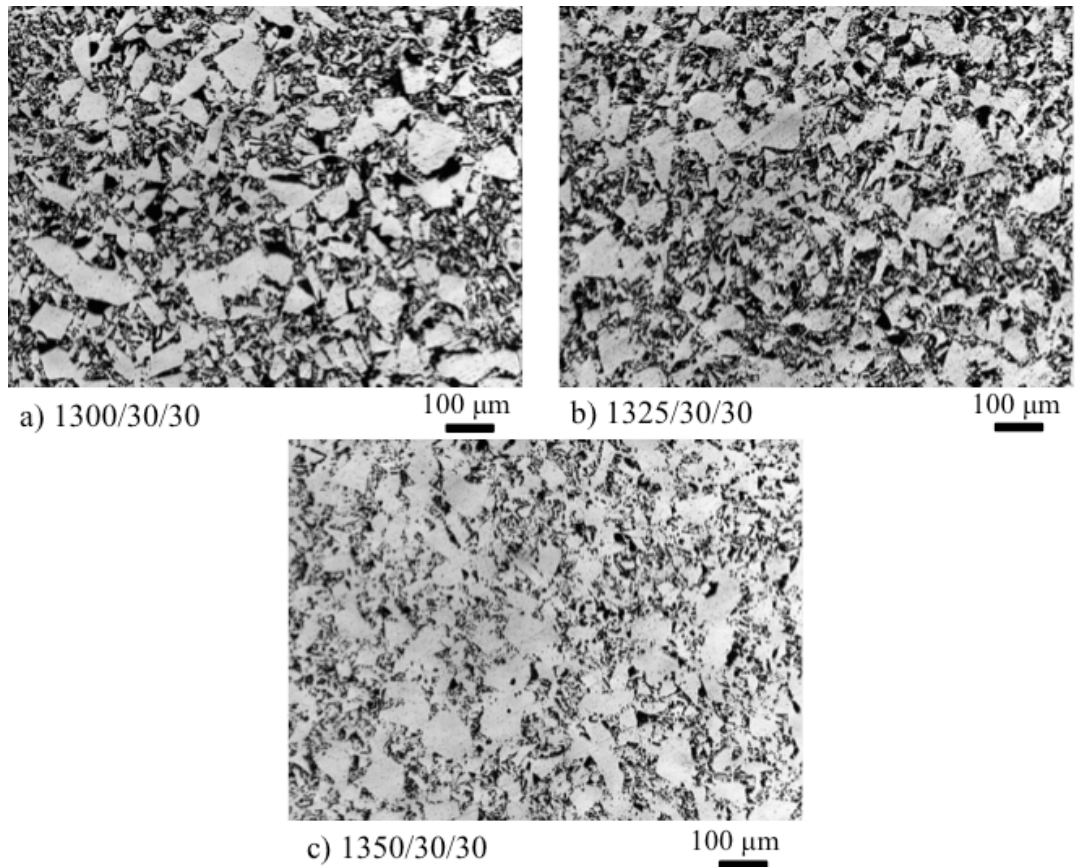
Figure 25 Light microscope images of samples conducted at 30 MPa and 30 minutes for three different temperatures (1300°C, 1325°C and 1350°C).

a) 1300/30/60 100 µm

b) 1325/30/60 100 µm

c) 1350/30/60 100 µm
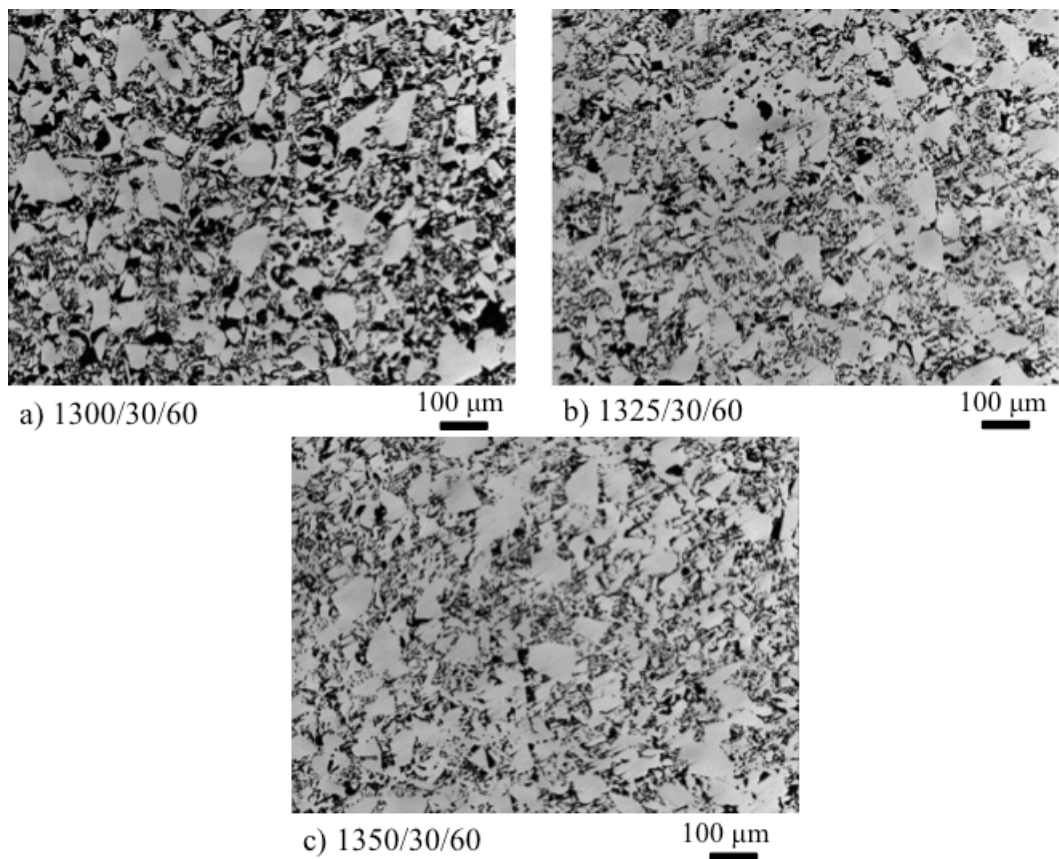
Figure 26 Light microscope images of samples conducted at 30 MPa and 60 minutes for three different temperatures (1300°C, 1325°C and 1350°C).

31

a) 1300/50/30   100 μm   b) 1325/50/30   100 μm

c) 1350/50/30   100 μm   d) 1375/50/30   100 μm
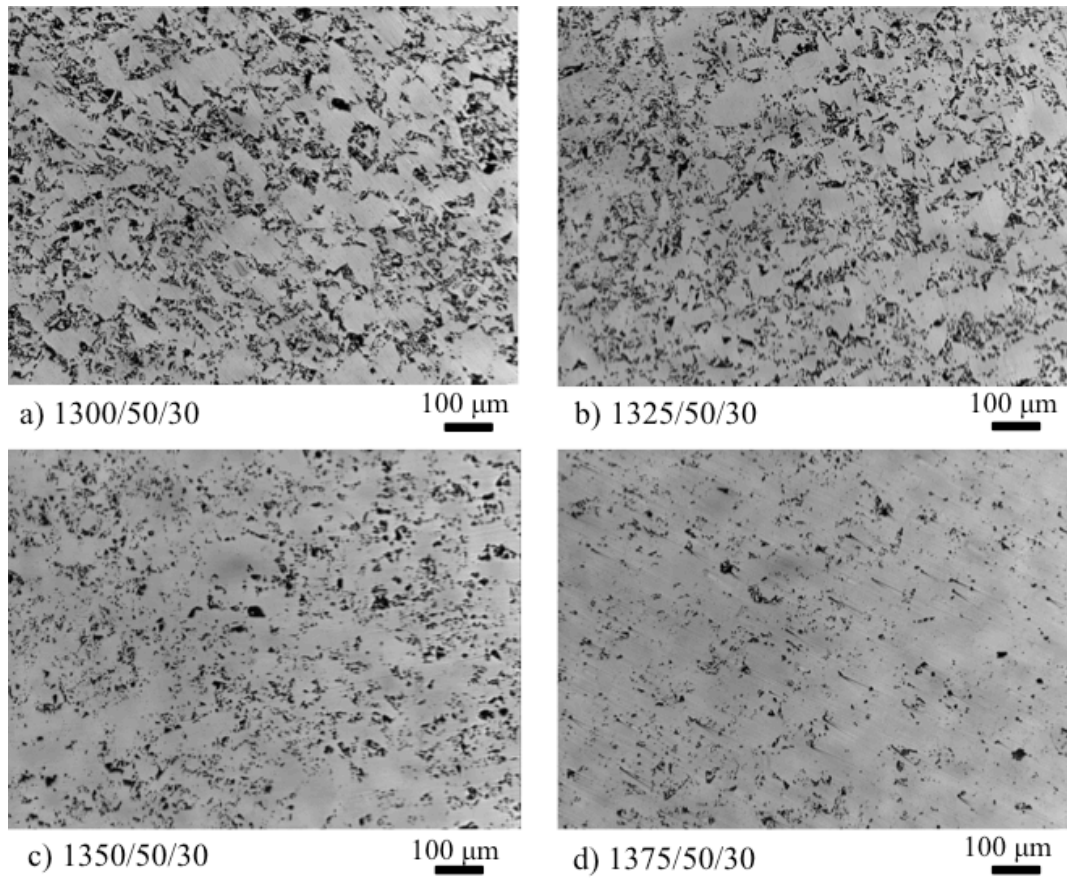
Figure 27 Light microscope images of samples conducted at 50 MPa and 30 minutes for four different temperatures (1300°C, 1325°C, 1350°C and 1375°C).

a) 1300/50/60   100 μm   b) 1325/50/60   100 μm

c) 1350/50/60   100 μm
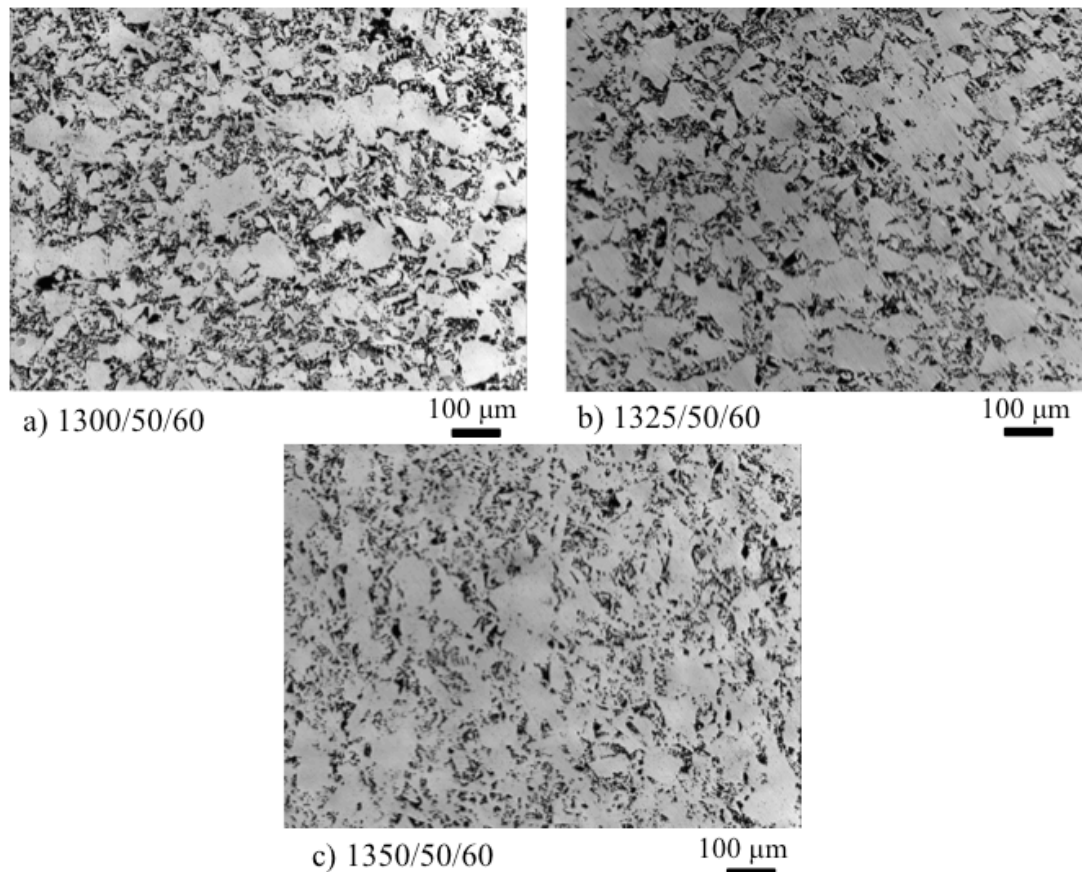
Figure 28 Light microscope images of samples conducted at 50 MPa and 60 minutes

4.3.3 Surface Porosity

The surface porosity was determined by using ImageAccess easyLab explained in 3.6.1. The average porosities of all the samples as function of temperature are given in Figure 29, while the inner and outer porosities are given in Figure 30.
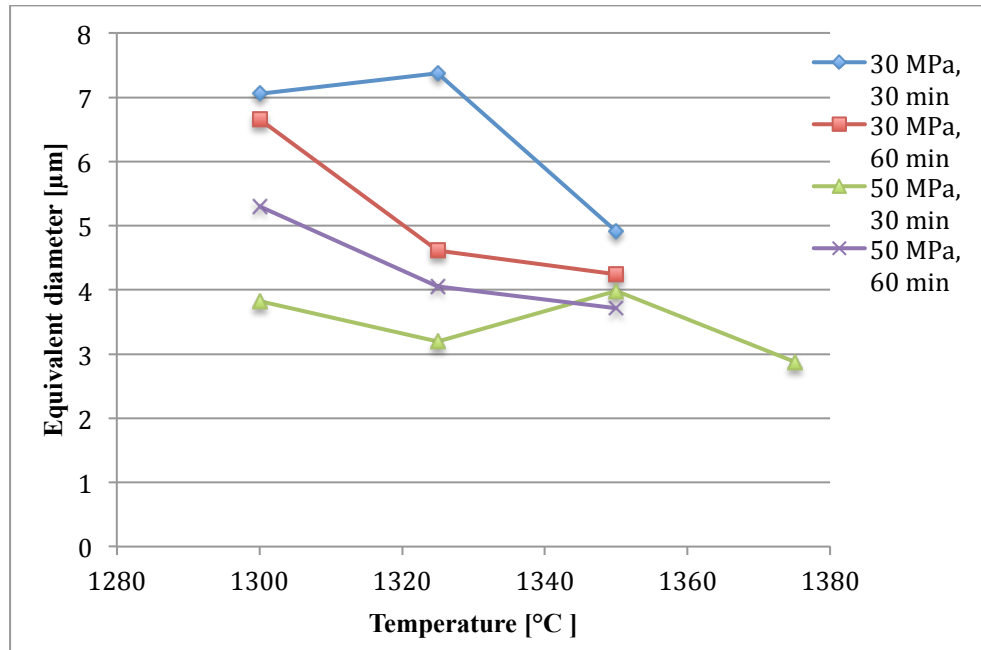
Figure 29 Equivalent diameter of porosities as function of temperature

Most of the samples have higher porosity in the inner part compared to the outer part. However for 1350/50/30 and 1350/50/60 the opposite is the case. Pellets conducted at 50 MPa show a significant decrease in surface porosity compared to those conducted at 30 MPa. This is in accordance with the density vs applied pressure curve in Figure 22.
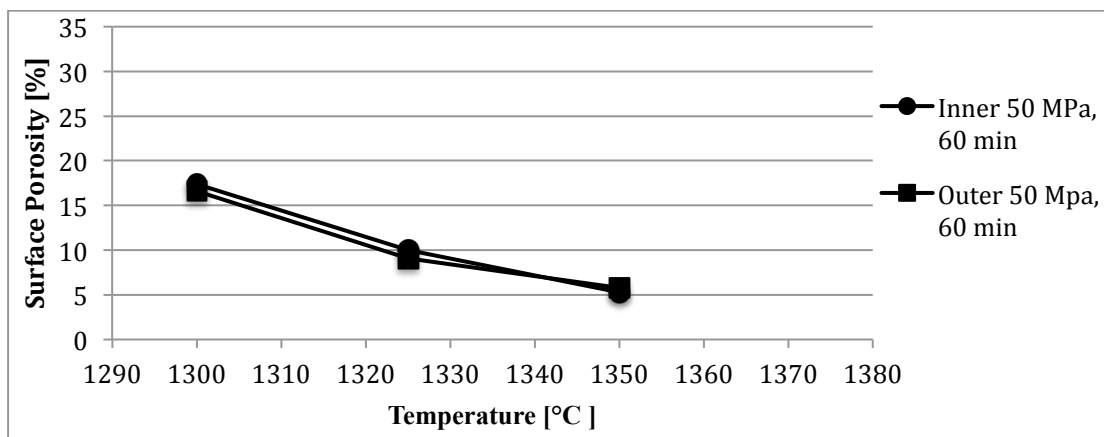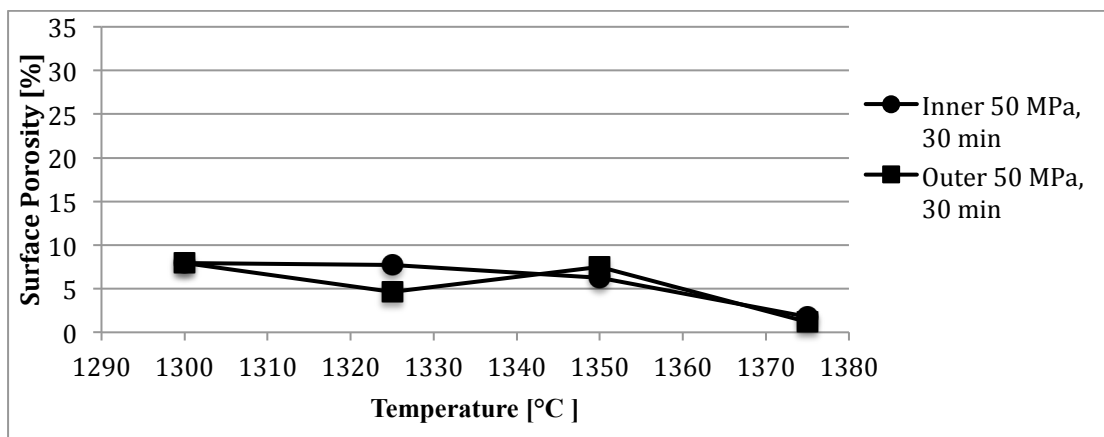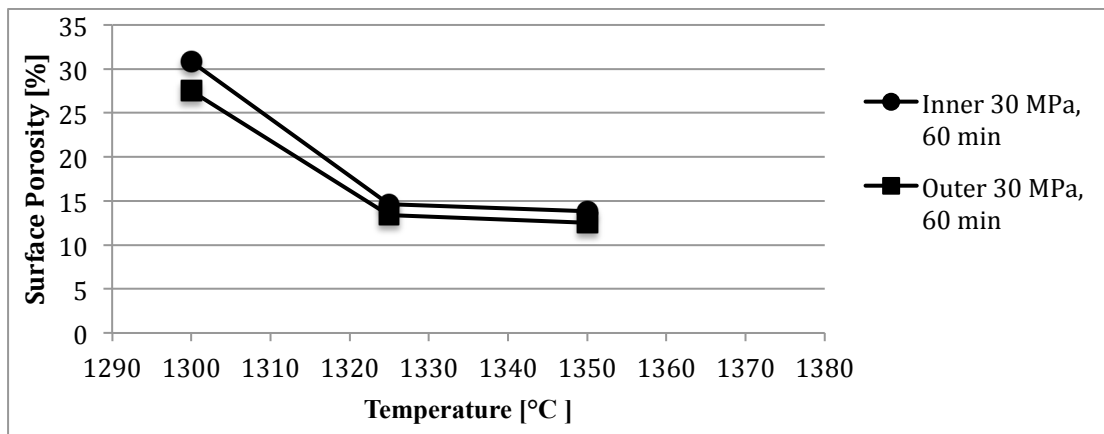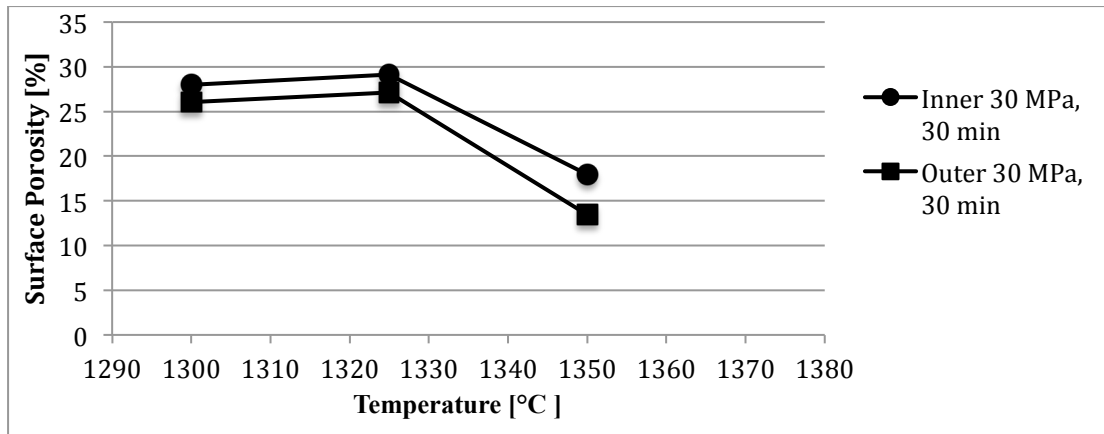
Figure 30 Surface porosity as function of temperature

The equivalent diameter of porosities as a function of temperature are presented in Figure 31 and Figure 32.
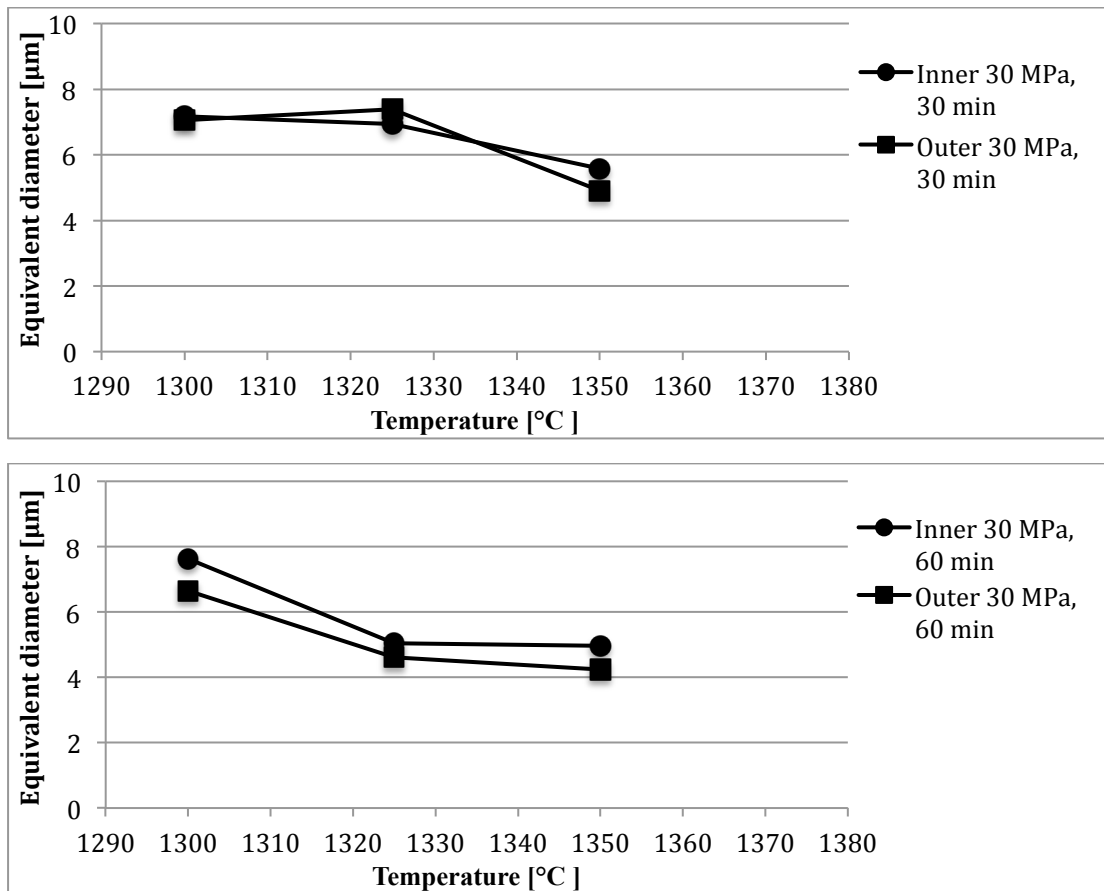
Figure 31 Equivalent diameter as function of temperature for X/30/30 and X/30/60.
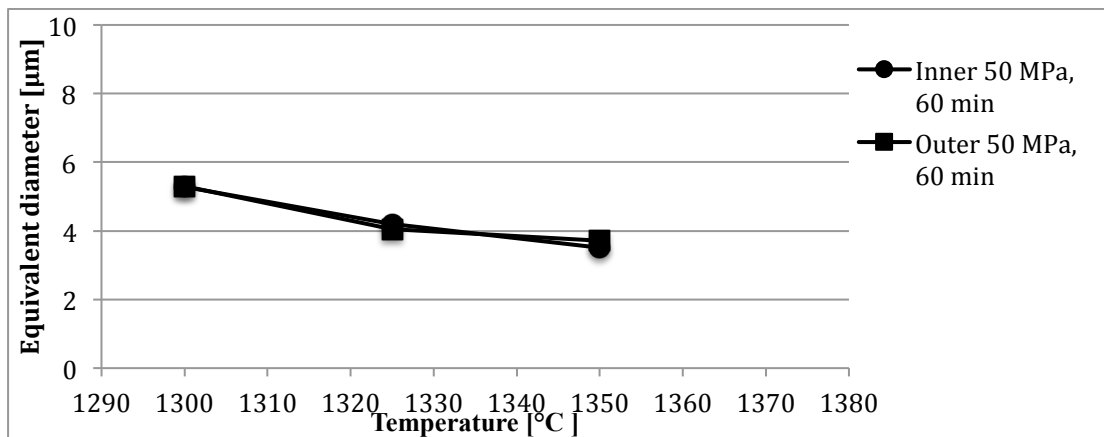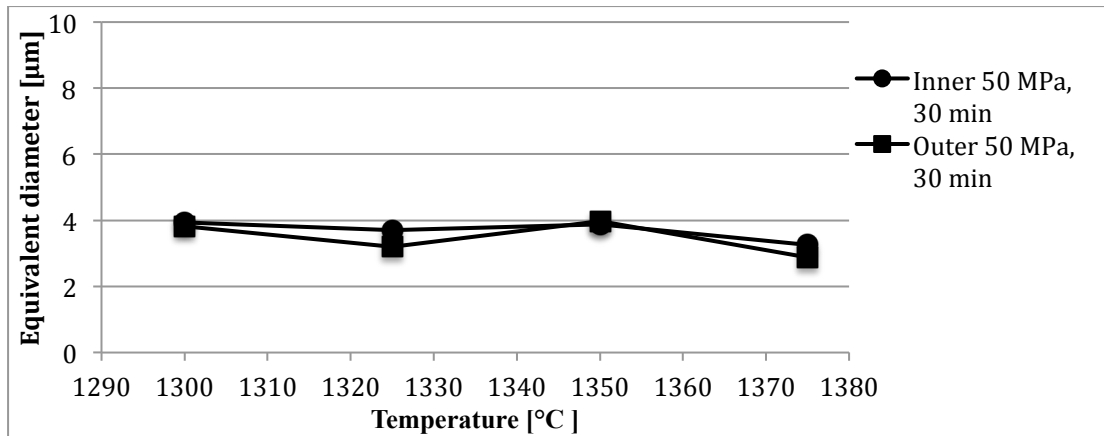
Figure 32 Equivalent diameter as function of temperature for X/50/30 and X/50/60.

Data for surface porosity, equivalent diameter and images from porosity analysis are given in Appendix C.

4.3.4 EBSD

EBSD of 1300/30/30, 1325/30/30 and 1350/30/30 before and after illumination with halogen lamps were carried out.

Figure 33-34 shows schematic of IPF and area fraction as function of grain size diameter before (a-b) illumination, and after (c-d) illumination by halogen lamps. Notice that the scale bar varies. The crystallographic orientations are very random, meaning that there is no preferred orientation. Each color in the IPF indicates the crystallographic orientation of the grains as described in 2.5.1.
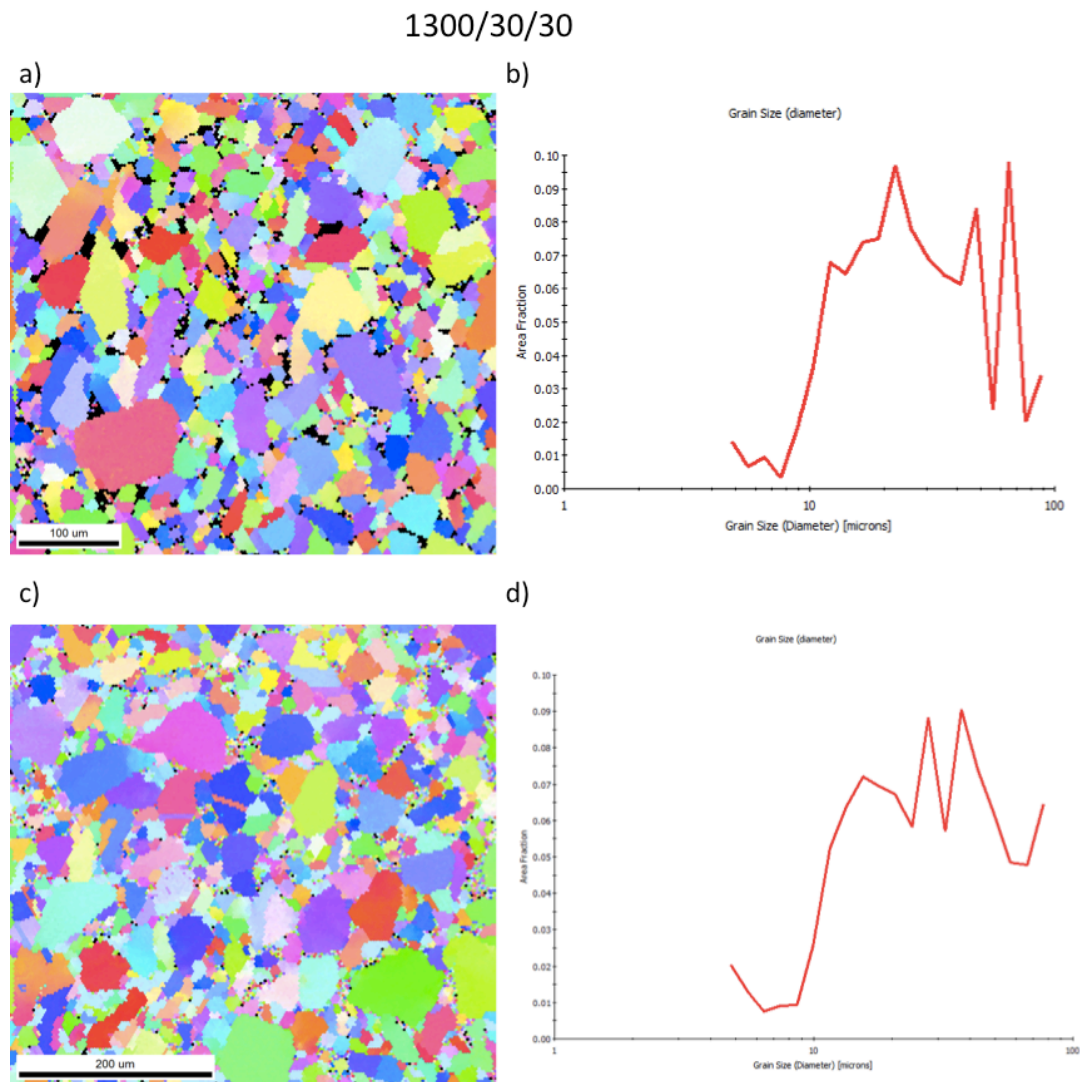
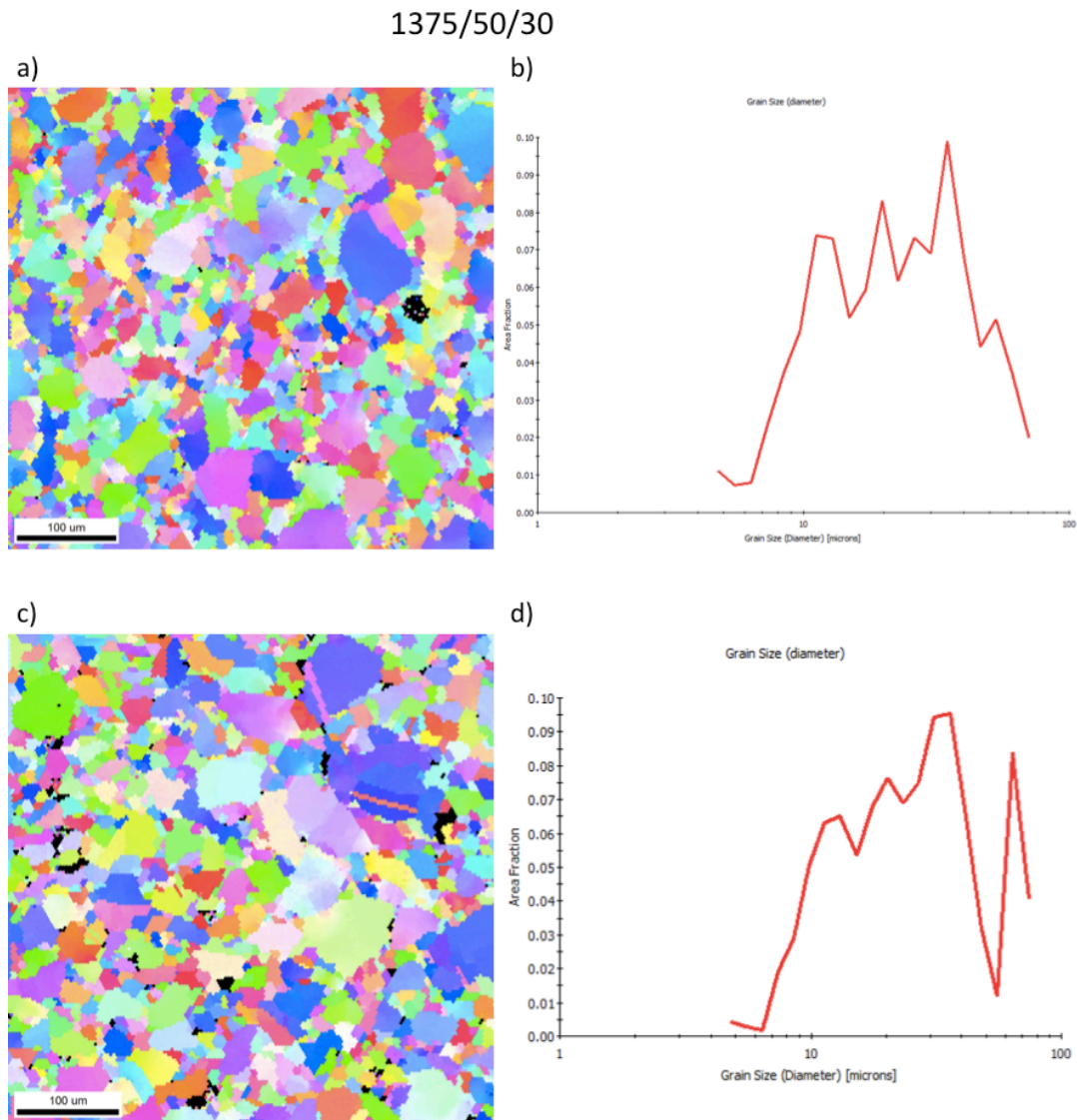**Figure 33 1300/30/30. a-b) IPF and grain size diameter before recrystallization. c-d) IPF and grain size diameter after recrystallization.**
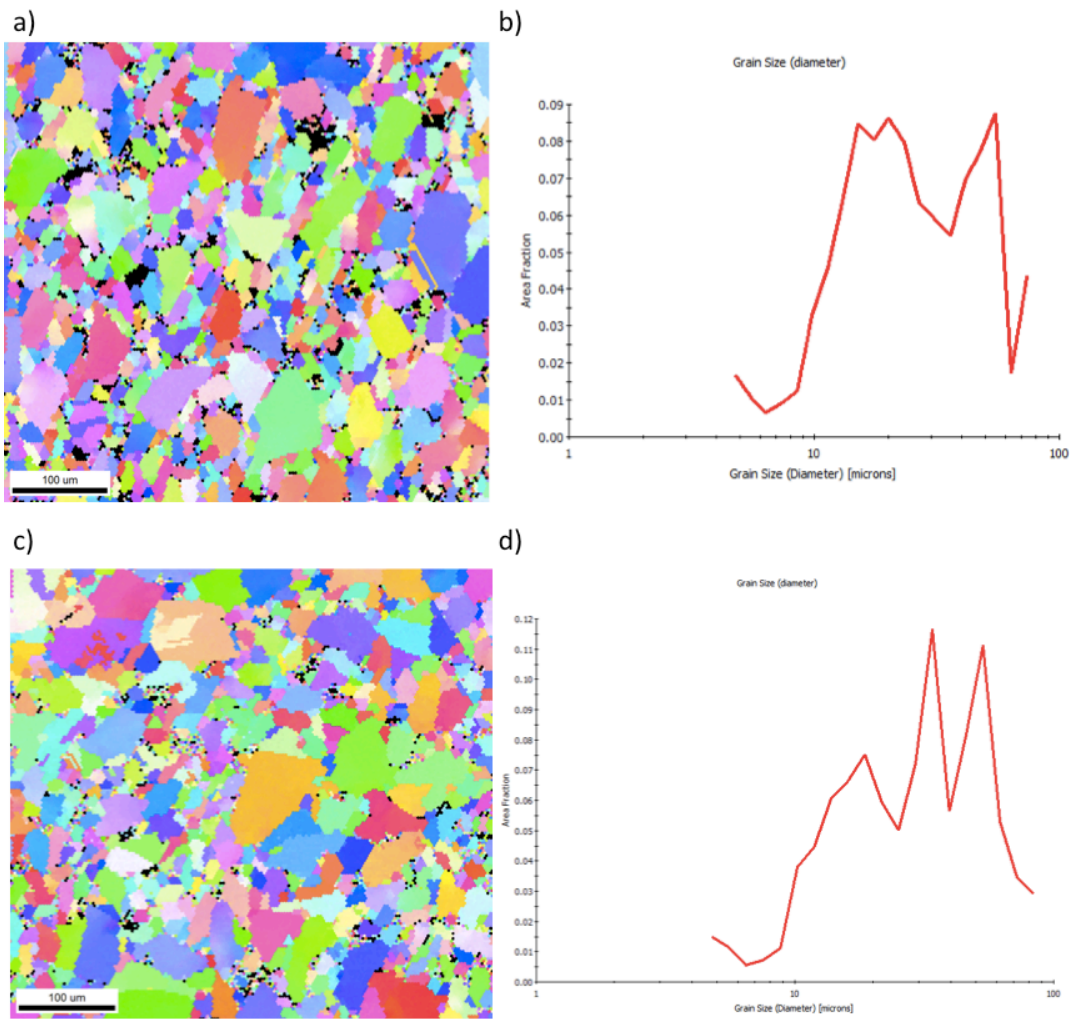
Figure 34 1325/30/30. a-b) IPF and grain size diameter before recrystallization. c-d) IPF and grain size diameter after recrystallization.

For 1300/30/30 and 1325/30/30 the average grain size was determined to 32,69 μm and 29,72 μm before illumination respectively, and 32,36 μm and 33,31 μm after illumination respectively. Comparing the two IPF images and graphs there are no abrupt changes in crystal orientations or grain size, meaning no recrystallization were achieved for these samples.

However indication of recrystallization was obtained for 1350/30/30. Figure 35 shows schematic of IPF and graph of area fraction as function of grain size before (Figure 35 a-b) illumination, and after (Figure 35 c-d) illumination by halogen lamps.

The average grain size before and after recrystallization increased from 31,83 μm to 56,96 μm which is a significant difference.
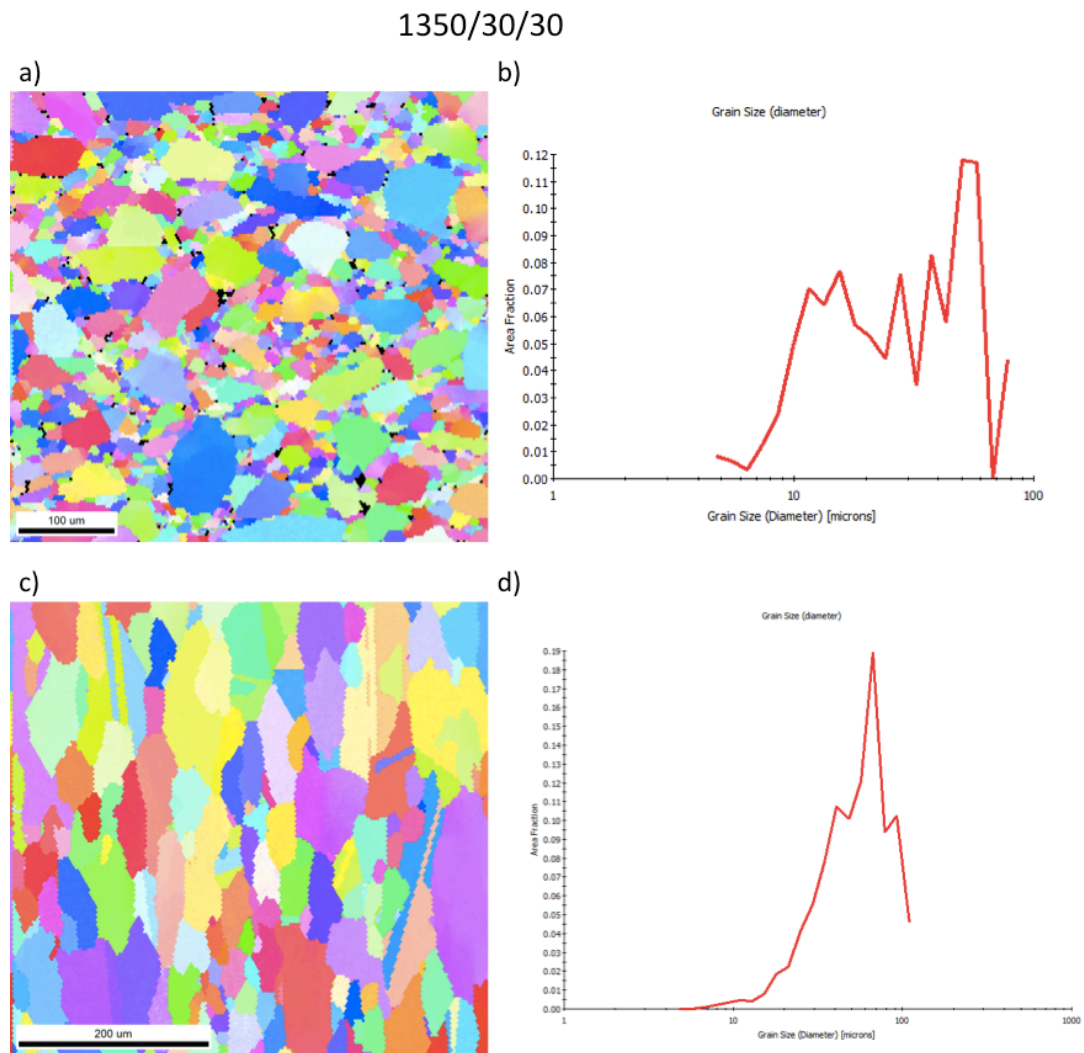
Figure 35 1350/30/30. a-b) IPF and grain size diameter before recrystallization. c-d) IPF and grain size diameter after recrystallization.

SEM pictures for 1350/30/30 before and after recrystallization showed elimination of porosity on the surface (Figure 36ab).
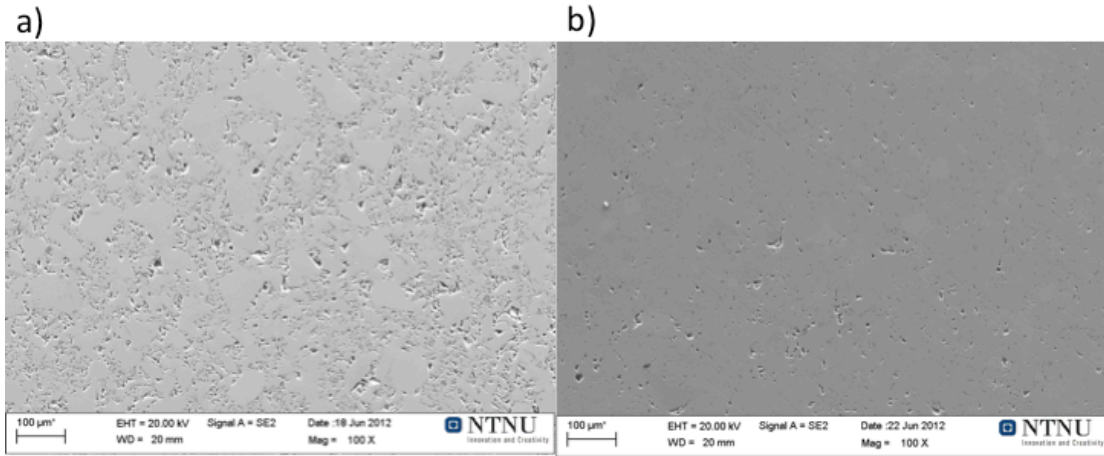
Figure 36 1350/30/30. a) Before recrystallization. b) After recrystallization

EBSD-tests were also carried out for 1350/50/30 and 1375/50/30 before and after illumination, but recrystallization was not achieved (see Figure 37 and Figure 38). The average grain size before and after illumination for 1350/50/30 was determined to 33,31 μm and 31,31 μm respectively.
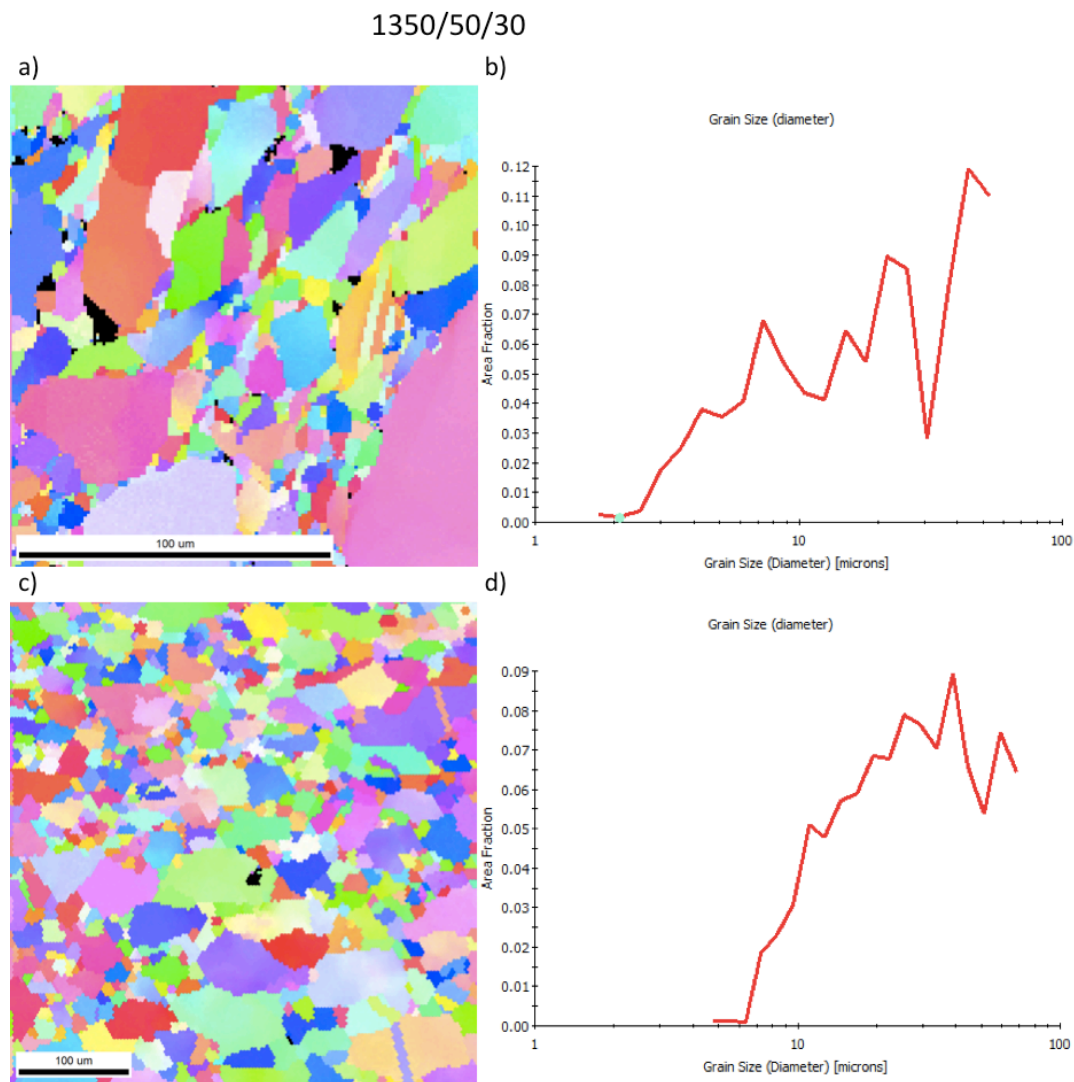
Figure 37 1350/50/30. a-b) IPF and grain size diameter before recrystallization. c-d) IPF and grain size diamter after recrystallization.

For 1375/50/30, the average grain size before and after illumination was determined to 30,31 μm and 29,37 μm respectively.

Figure 38 1375/50/30. a-b) IPF and grain size diameter before recrystallization. c-d) IPF and grain size diamter after recrystallization.

4.4   Resistivity and conductivity

Conductivity was measured in accordance with SIGMATEST 2.069 and is presented in Figure 39. Conductivity data were used to calculate resistivity by using equation 2.6.

From Figure 39, the resistivity increases with maximum hot-pressing temperature, meaning that the conductivity decreases with increasing maximum hot-pressing temperature.
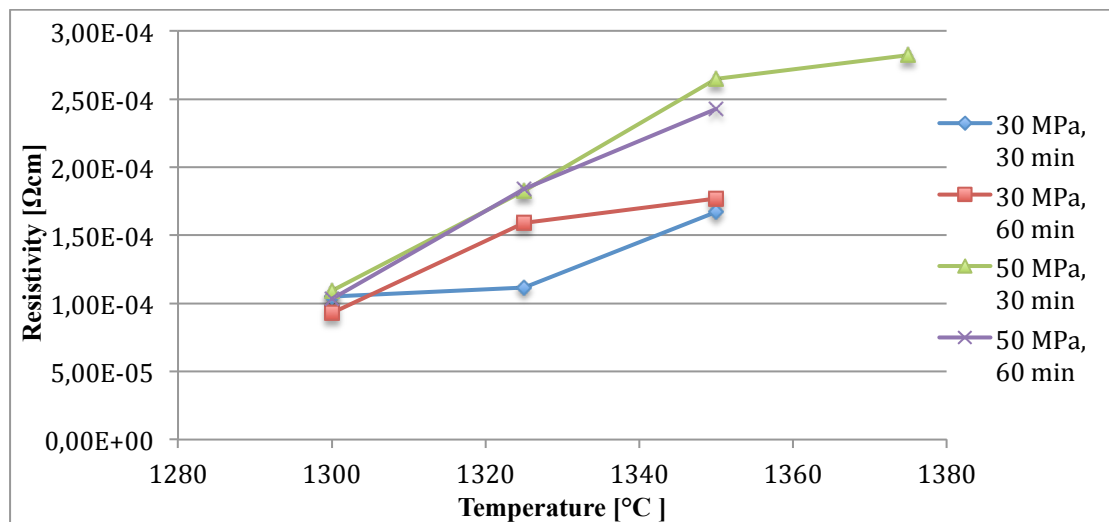
Figure 39 Resistivity as function of temperature.

Resistivity as function of applied pressure for 30 and 60 minutes is illustrated in Figure 40.
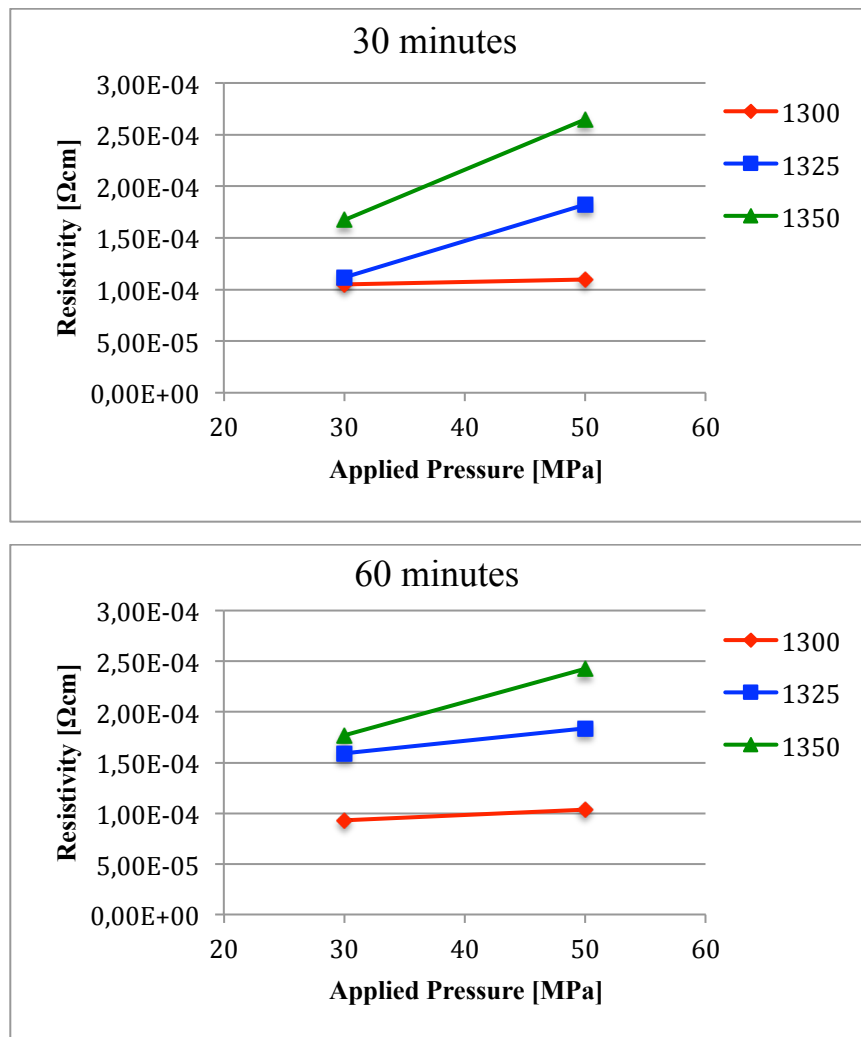
Figure 40 Resistivity as function of applied pressure for 30 and 60 minutes

The results from the SIGMATEST 2.069 showed that the resistivity at the center of the circular was higher compared to the resistivity at the outer edge of the pellets, see Table 2

Table 2 Variation in conductivity at inner and outer part of the pellet

Sample	Inner Resistivity [Ωcm]	Outer Resistivity [Ωcm]
1300/50/30	1,58E-04	6,08E-05
1325/50/30	2,01E-04	1,64E-04
1350/50/30	2,92E-04	2,38E-04
1375/50/30	2,99E-04	2,65E-04
1300/30/30	1,37E-04	7,30E-05
1325/30/30	1,53E-04	7,07E-05
1350/30/30	2,34E-04	1,01E-04
1300/30/60	1,06E-04	8,05E-05
1325/30/60	1,97E-04	1,21E-04
1350/30/60	2,23E-04	1,31E-04
1300/50/60	1,28E-04	7,82E-05
1325/50/60	2,34E-04	1,34E-04
1350/50/60	2,76E-04	2,09E-04

5 Discussion

5.1 Densification behavior

For the pellets hot-pressed at constant pressure and time, only varying temperature, the density increased with temperature. It can be concluded that the temperature has a major role in promoting diffusion and giving high densities. X/50/30 and X/50/60 resulted in highest densities. Comparing these two with each other, the density was nearly identical at the same temperatures.

Taking the pressure sintering time in consideration, 1325/50/60 and 1325/50/30 showed a variation in density of 2,45 %. For 1350/50/60 and 1350/50/30, and X/30/30 and X/30/60, the difference was even lower. From this it can be concluded that the pressure sintering time does not have any major effect on the density. The decreasing rate of densification is reached at a time > 30 minutes. This is in agreement with Figure 4 where there is a decreasing rate of densification with increasing time [12]. From the literature the density of the pellets increases linearly with pressure. In this thesis, only 30 MPa and 50 MPa were applied, and there is not sufficient data to say if there is a linear behavior. It is therefore interesting to look at one more pressure parameter (e.g 40 MPa) to see if there is any linear coherence with respect to density and pressure.

Based on Figure 3, pressure is most useful in elimination of pores if the grain size is large with respect to the pore size.

However, 1300/30/60 and 1300/30/30 showed lower and approximately the same density respectively compared to 1200/50/30, which is a contradiction. This can be explained by a challenging step during the densification experiment.

A critical and challenging step when performing the Archimedes' Principle test is to measure the weight of the pellet in air while it is still soaked with the liquid. This is done by immediately wiping off the pellet quickly and carefully with a smooth cloth to remove droplets on the surface without drawing liquid out of any of the pores. This was quite challenging since the dimension of the pellets was relative large, and therefore can cause incorrect measurements. The result should be more accurate for a pellet of smaller dimensions.

5.2 Hot-pressed sample at 1200 °C

The first successful solid sample was carried out at 1200/50/30, see Figure 41. As can been seen, the surface is very porous and this is in accordance with the density of 1,90 g/cm^3 determined from Archimedes Principle. The SIGMATEST did not give any values indicating that the sample was an insulator. This is might due to that no neck formation at the contact point between each particle was obtained due to low temperature, meaning that the particles were just pressed together with an oxide layer of silica on each powder particle. The SiO$_2$ acts as an electric insulator with high chemical stability [3]. This limits the current flow of electrons.
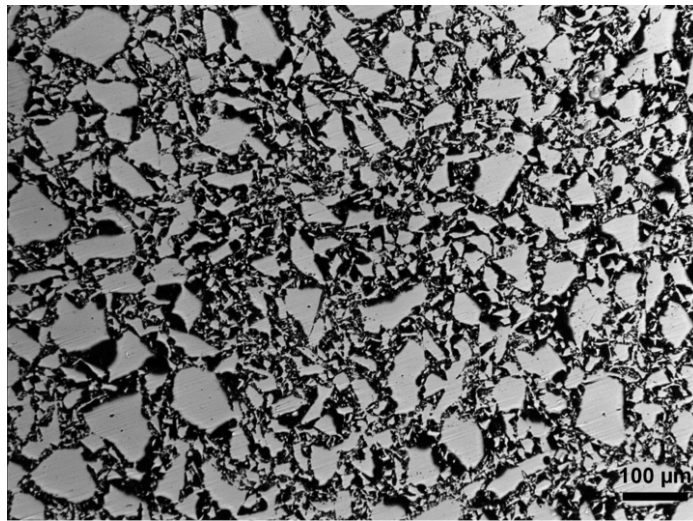
Figure 41 Hot-pressed sample at 1200 showing porous surface.

This was the only sample hot pressed at 1200 °C, because based upon the data given above, it was expected that varying pressure and sintering time would not change the properties significantly with respect to resistivity and therefore not be of any interest for suitable substrates for thin film solar cells.

5.3 Issues with Hot-pressed pellets

There were times were the pellet tended to fracture when pulling it out of the die. Two types of fracture were observed (Figure 42a-b). It split into two pieces, or it just let off some flakes on one of the surfaces.
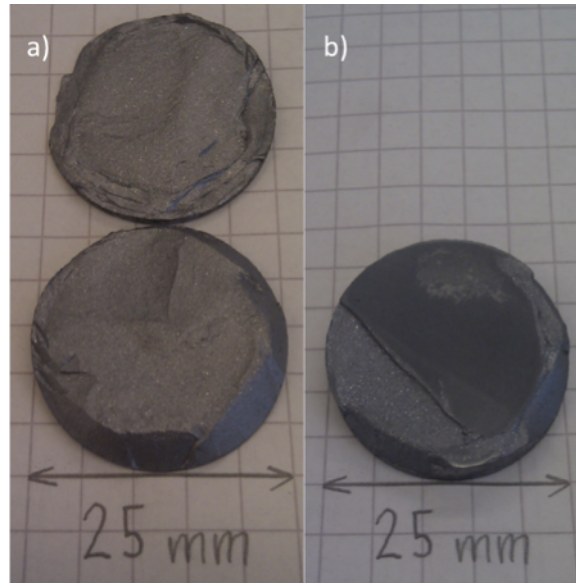
Figure 42 Two types of fracture were observed. a) The pellets cracked into two separate pieces. b) The pellet lost some flakes on the surface.

In the beginning, this occurred for tree pellets hot-pressed at 1375 °C, and it was assumed that high temperature was the main reason for the fracture behavior. Therefore no further hot-pressing at such high temperatures was conducted.

However, later on, this also occurred for lower temperatures when there were only two remaining samples to press. It was then observed that the inside wall of the graphite which had been used several times had a rough surface inside the cylinder wall, see Figure 43. It is suggested that this is due to radial constraint from the die wall during hot-pressing [12].
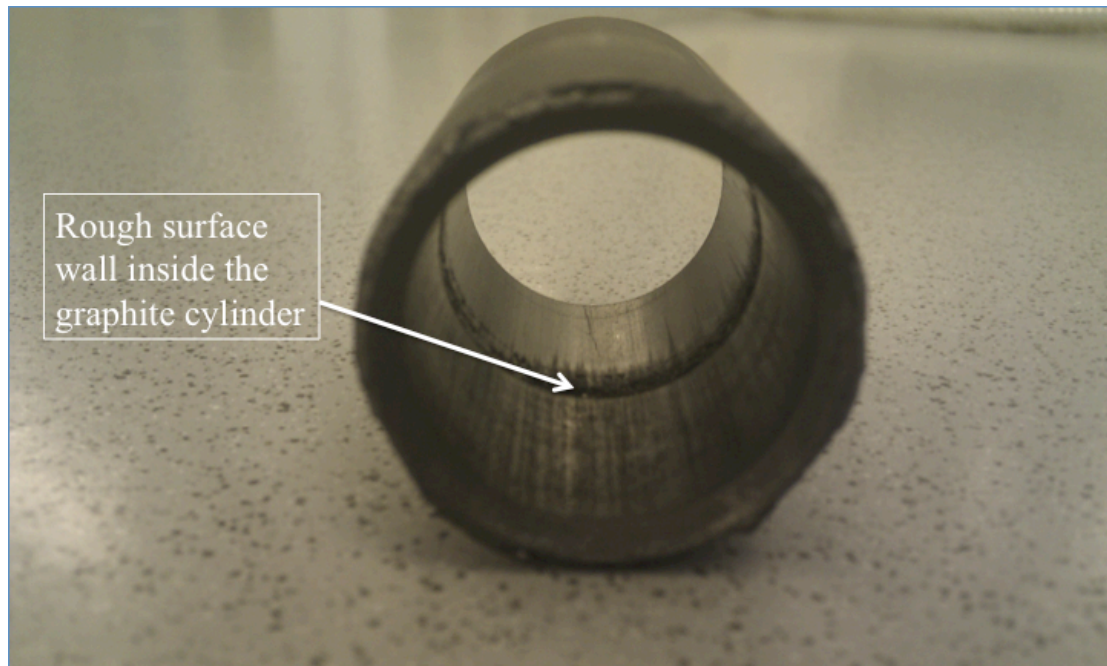
Figure 43 When using same graphite cylinder for several pellets, a rough surface wall seemed to occur inside the graphite die, making it hard to pull the pellet out without causing fracture on the sample.

It was also observed on the pressure gauge for pellets that fractured, that pressures above 1000 kg had to be applied before the pellet was unattached from the graphite cylinder wall. In addition, relative loud friction sounds occurred when pulling the pellet out of the cylinder.

The cylinder in Figure 43 was used 6 times before the pellets partially fractured and let off flakes on one surface. It was therefore replaced with a new one during the next hot-pressing, and when pulling it out, the gauge pellet showed approximately 500 kg before pellet was released. This pellet showed desired geometry without any fracture. It is therefore important to be observant and to pay great attention to the graphite cylinder. When synthesizing pellets using this method, it seems like the cylinder can be used 5-6 times before a new one must be replaced to avoid fracture. A solution is to spray the inside cylindrical wall with BN, that will prevent sticking, but not necessarily the rough surface.

5.4 Surface porosity and equivalent diameter

At constant temperature and time, only varying the pressure, lower pressure resulted in higher porosity fraction by an order of at least 2. The inner surface porosities of 1300/30/30 and 1300/50/30 were 27,98 % and 7,95 % respectively which is an order of 3,5. It can be concluded that higher pressures and temperatures accelerate the

densification process and pore shrinkage [12]. This can be seen from the equivalent diameter results in Figure 31 and Figure 32, and from optical microscopy images in Figure 25-27.

The densest pellets were obtained at high applied pressures and temperatures. 1375/50/30 showed a density of 2,239 g/cm^3 which is close to 100% theoretical densification of silicon. From EBSD, the average grain size was determined to 30,31 μm, while the equivalent diameter (average of inner and outer diameter) was determined to 3,07 μm. Grain size is large with respect to the pore size and pressure is useful in elimination of pores [12]. This is also true for the 1300/30/30, 1325/30/30 and 1350/30/30 (all with grain size ~30 μm) and average equivalent diameter of 7,12 μm 7,16 μm and 5,25 μm.

Most of the samples had higher porosity in the inner part compared to the outer part. The exceptions were 1350/50/30 and 1350/50/60 where the porosities at the outer part were 16,91 % and 8,65 % higher respectively compared to the inner part.
It should be noticed that only one image has been taken for the inner and outer part, and therefore the values are not very representative. Taking more images from both inner and outer part followed by pore analysis, and then determine the average surface porosity should give more representative and reliable values. This does not mean that higher porosities at the inner parts are expected for all samples, but still the values will be more representative.

An increase in applied pressure resulted in smaller pores. For example 1300/50/30 and 1300/30/30, the equivalent diameters of the pores were determined to 3,93 μm and 7,18 μm respectively. The differences decreased as the temperature increased. For 1350/50/30 and 1350/30/30 the diameters were determined to 3,88 μm and 5,58 μm respectively. This is reasonable since the fraction of surface porosity was much higher for samples hot-pressed at lower applied pressure (when temperature and time is constant).

5.5   EBSD

IPF from EBSD showed that the hot-pressed samples had an average grain size of approximately 30 μm. From the laser diffraction analysis the mean particle size was

determined to 20,36 μm. It can be concluded that low grain growth occurred during pressure sintering [10, 14].

EBSD was used for characterization of microstructure, primarily to determine grain size before and after illumination. It turned out to be a very time consuming technique, and therefore EBSD was not performed on all the samples due to time limitations. For characterization of microstructure and crystalline defects it is more time efficient to etch the sample. For silicon, Secco etch is a rapid chemical method [31]. The composition is hydrofluoric acid (HF), 67% by volume and 0,15M $K_2Cr_2O_7$ in H_2O, 33% by volume [32].

5.6   Recrystallization

Recrystallization of the samples was not successful, except for 1350/30/30. For this sample the high temperature caused large grains to grow on the expense of small grains, increasing the average grain size after recrystallization.

The illuminated samples were ~2,5 mm thick. Before illumination the sample was put horizontally with one side down on top of a tungsten plate.

P.Bellaner et. al [24] had micron thick samples and kept the sample vertically thanks to adequate support, and on both sides, two elliptic mirrors focused the radiation from the lamps. Also the process was made under argon flow.

A. Draoua et. al had samples with thicknesses between 300 and 600 μm. In addition the halogen lamps apparatus was very advanced (provided by Freiburg ISE). The process was computer controlled, which allowed a very reproducible process while retaining high variability and control of process parameters [8].

The equipment used in this study was rather simple and manual with no control over the parameters with respect to homogenous radiation on the surface specimen or heating and cooling rates. Despite of this, recrystallization was successful for 1350/30/30 in normal atmosphere.

It is hard to determine the factors for failure of the samples conducted with respect to recrystallization, except from 1350/30/30, but by comparing the known parameters from the articles described above and this study, the thickness and homogeneous illumination on both sides of the sample probably plays an important role.

5.7 Conductivity and resistivity

According to the SIGMATEST, the resistivity was higher at the center part compared to the outer part of the pellet. This can be related to the fact that the surface porosity was higher at the center (except from 1350/50/30 and 1350/50/50) causing more scattering of electrons, which is the main cause of resistivity. Structural imperfections present in the solid also contribute to resistivity. These are mainly defects such as dislocations and grain boundaries [21].

From Table 3, the contamination of Al and B are measured to 21 and 0,3 ppmw respectively. Al is regarded as p-type doping since it gives rise to a hole tied to the group atom.
By assuming Al impurities as B impurities, assumption of the resistivity can be found in Figure 6.
ppmw can be converted to cm^{-3} by equation 5.1.

$$\frac{ppmw \times \rho_{Bor} \times N_A}{M_{w,Bor}} \qquad 5.1$$

where ppmw is parts per million weight, ρ_{Boron} is the theoretical density of boron, N_A is Avogadro constant and $M_{w,Boron}$ is the molar weight of boron.
By using data from Table 3 and equation 5.1, 21,3 ppmw equals a dopant density of $2,78 \times 10^{18}$cm^{-3}. From Figure 6, this gives a resistivity of $\sim 1,6 \times 10^{-2}$ Ωcm, which is a magnitude of 2 larger than for the resistivity measurements by the SIGMATEST in this study. Professor Alexander Ulyashin at SINTEF Oslo, measured the resistivity of 1350/50/30 by 4-point probe which gave the following result of $1,75 \times 10^{-3}$ Ωcm. This is 1 order of magnitude from the result with respect to the SIGMATEST, but is considered as more accurate because it is mainly used on semiconductors to measure the total impurity content of a sample [33]. By consider the Al-impurity as B-impurity, an approximation of the resistivity can be proposed with respect to the 4-point probe measurement.

6 Conclusions

Hot-pressing silicon powder to pellets proved to be successful. Densities in between 90 - 96 % were obtained at high temperatures and pressures. The time (30 and 60 minutes) conducted at maximum temperature during hot-pressing was not of vital importance with respect to density.

The applied pressure and relatively low temperature limited grain growth to ~30 μm and yielded fine microstructure.

ZMR proved to be successful for 1350/30/30 with very simple and manual device in normal atmosphere, with elimination of pores and significant grain growth from 31,83 to 56,96 μm.

7 Further Work

- Recrystallize by annealing in hot-pressing in inert atmosphere. After hot-pressing the sample is subsequently annealed in the hot-press furnace by applying a steep temperature gradient between front and back surfaces.

- Fabricate new dies that can hot-press larger pellets (~ 25 cm^2), but with thicknesses in the micron range.

- Etch samples to (e.g Secco Etchant) reveal grain boundaries and dislocations. Characterization of grain boundaries and dislocation with respect to resistivity should be interesting.

- Apply a flow of argon on the surface of the samples during recrystallization by halogen lamps to reduce oxidation reactions.

- Use a mixture of H_2 (≈ 5 %) and Ar in the furnace during hot-press to evaporate the native oxide layer from the silicon powder.

References

1. Ishihara, T., et al., *Zone-melting recrystallization of silicon thin films for solar cell application.* Progress in Photovoltaics: Research and Applications, 1995. **3**(2): p. 105-113.
2. Ulyashin, A.G., *Thin Si film based hybrid solar cells on low-cost Si substrates.* 2009: p. 84.
3. Grau, M., et al., *High Voc Crystalline Silicon Thin Film Solar Cells through Recrystallised Wafer Equivalent Applied to Sintered Silicon.* 2009.
4. J. McCann, M., et al., *A review of thin-film crystalline silicon for solar cell applications. Part 1: Native substrates.* Solar Energy Materials and Solar Cells, 2001. **68**(2): p. 135-171.
5. Hamakawa, Y., *Thin-film solar cells: next generation photovoltaics and its applications*2004, Berlin: Springer. XV, 244 s.
6. Fraas, L. and L. Partain, *Solar Cells and Their Applications.* Second ed2010: John Wiley & Sons.
7. Brendel, R., *Thin-Film Crystalline Silicon Solar Cells: Physics and Technology*2003: Wiley. 306.
8. Reber, S., W. Zimmermann, and T. Kieliba, *Zone melting recrystallization of silicon films for crystalline silicon thin-film solar cells.* Solar Energy Materials and Solar Cells, 2001. **65**(1–4): p. 409-416.
9. Yin, Q., B. Zhu, and H. Zeng, *Microstructure, Property and Processing of Functional Ceramics*2010, Berlin, Heidelberg: Springer-Verlag Berlin Heidelberg.
10. Ricerhson, D.W., *Modern Ceramics Engineering: Properties, Processing and Use in Design.* Third ed2006: Taylor & Francis.
11. Bengisu, M., *Engineering Ceramics*2001: Springer.
12. German, R.M., *Sintering Theory and Practice*1996: Wiley.
13. Askeland, D.R. and P.P. Phulé, *The Science and Engineering of Materials.* Fifth ed2008: Cengage Learning.
14. Czepelak, M., et al., *Fabrication of nano-structured material by high-pressure sintering.* 2008.
15. Kakar, A.K. and A.C.D. Chaklader, *Deformation Theory of Hot‐Pressing.* Journal of Applied Physics, 1967. **38**(8): p. 3223-3230.
16. Gilman, P.S. and G.H. Gessinger, *A Method for the Experimental Determination of the Effective Stress in Hot Pressing* 1980.
17. Carlson, R.G. and F.E. Westermann, *Hot Pressing of Lead Spheres.* 1962.
18. Raj, R., *Analysis of the Sintering Pressure.* Journal of the American Ceramic Society, 1987. **70**(9): p. C-210-C-211.
19. Draoua, A.D., et al., *Production of MC-Silicon wafers by sintering of silicon bed powders and subsequent re-crystallization.* 2010.
20. ISO, *Dense shaped refractory products - Determination of bulk density, apparent porosity and true porosity*, in *5017*1998.
21. Tilley, R.J.D., *Understanding Solids: The Science of Materials*2004: J. Wiley.
22. Standard, A., *Standard Practice for Conversion Between Resistivity and Dopant Density for Boron-Doped, Phosphorus-Doped, and Arsenic-Doped Silicon*, 1999.

23. Green, M.A., *Solar cells: operating principles, technology, and system applications*1982: Prentice-Hall.

24. Bellanger, P., M. Grau, and A. Sow, *Multicrystalline Silicon wafers prepared by sintering of silicon bed powders and re-crystallization using ZMR.* 2009.

25. Williams, T.J., *Scanning electron microscopy and x-ray microanalysis, 3rd edition. By Joseph Goldstein, Dale Newbury, David Joy, Charles Lyman, Patrick Echlin, Eric Lifshin, Linda Sawyer, Joseph Michael Kluwer Academic Publishers, New York (2003) ISBN 0306472929; hardback; 688; $75.00.* Scanning, 2005. **27**(4): p. 215-216.

26. Hjelen, J., *Scanning elektron-mikroskopi.* Metallurgisk institutt, 1989.

27. Schwartz, A.J., M. Kumar, and B.L. Adams, *Electron Backscatter Diffraction in Materials Science*2009: Springer.

28. Zhou, W. and Z.L. Wang, *Scanning Microscopy for Nanotechnology Techniques and Applications* 2007.

29. Geels, K., *Metallographic and materialographic. Specimens preparation, Light Microscopy, Image Analysis and Hardness Testing*2007: ASTM International.

30. *Precision Ellipsoidal Reflectors*. 2012; Available from: http://www.edmundoptics.com/optics/optical-mirrors/focusing-concave-mirrors/precision-ellipsoidal-reflectors/3091.

31. Younan, H., *Studies of A New Chemical Etching Method - 152 Secco Etch in Failure Analysis of Water Fabrication.* 1998.

32. Secco, F.d.A., *Dislocation Etch for (100) planes in silicon.* Journal of the Electrochemical Society, 1972. **119**(7): p. 948-951.

33. *Four Point Probe Theory*. Available from: http://www.fourpointprobes.com/fpp.html.

Appendix A

Table 3 Impurity data measured in ppmw (parts per million weight)

	B (ppmw)	Fe (ppmw)	Al (ppmw)	Ca (ppmw)
Si powder	0,3	31	21	442

Appendix B

Determination of Density and Porosity from Archimedes' Principle

Table 4 shows the data for weight of dry sample, wet sample immersed in isopropanol and sample in air, in addition to the temperature for $\rho_{isoprop.}$

Table 4 Measured values from Archimedes principle.

Sample	Temp. [°C]	m_1 [g]	m_2 [g]	m_3 [g]	Temp. Isoprop. [°C]
1200/50/30	1200	4,8726	3,2289	5,2401	17
1300/50/30	1300	5,0108	3,3259	5,2965	17
1325/50/30	1325	4,8298	3,2027	4,9687	22
1350/50/30	1350	5,0485	3,3458	5,1783	19
1375/50/30	1375	4,6042	3,0177	4,6311	19
1300/30/30	1300	4,9888	3,3141	5,3630	21,5
1325/30/30	1325	4,9137	3,2609	5,2440	21,5
1350/30/30	1350	4,9765	3,2757	5,1640	21,5
1300/30/60	1300	4,9263	3,2682	5,3190	19
1325/30/60	1325	4,8615	3,2252	5,1330	19
1350/30/60	1350	4,6425	3,0729	4,8810	19
1300/50/60	1300	4,8742	3,2349	5,1471	19
1325/50/60	1325	4,9989	3,3172	5,1973	19
1350/50/60	1350	4,9563	3,2716	5,0578	19

The bulk density, apparent porosity and true porosity were determined in accordance with ISO 5017:1998 by using equation 2.1-2.4. The calculated values are presented in Table 5.

Table 5 Calculated data from Archimedes' Principle

Sample	$\rho_{isoprop}$ [g/cm³]	ρ_b [g/cm³]	π_a [%]	π_t [%]
1200/50/30	0,7865	1,9055	0,00	18,18
1300/50/30	0,7865	1,9999	0,00	14,13
1325/50/30	0,7820	2,1387	0,00	8,17
1350/50/30	0,7847	2,1618	7,08	7,18
1375/50/30	0,7847	2,2393	1,67	3,85
1300/30/30	0,7825	1,9053	18,26	18,19
1325/30/30	0,7825	1,9389	16,66	16,75
1350/30/30	0,7825	2,0622	9,93	11,45
1300/30/60	0,7847	1,8850	19,15	19,07
1325/30/60	0,7847	1,9996	14,23	14,14
1350/30/60	0,7847	2,0148	13,19	13,49
1300/50/60	0,7847	2,0002	14,27	14,12
1325/50/60	0,7847	2,0864	10,55	10,42
1350/50/60	0,7847	2,1774	5,68	6,51
1350/50/30	0,7861	2,1544	7,35	7,49

The density for isopropanol ($\rho_{isoprop}$) in g/cm³ at the current temperature was calculated according to equation A.1 given below.

$$\rho_{isoprop} = -0,0009T + 0,8018 \qquad (A.1)$$

where T is the temperature of isopropanol in centigrade. The graph is given in Figure 44.
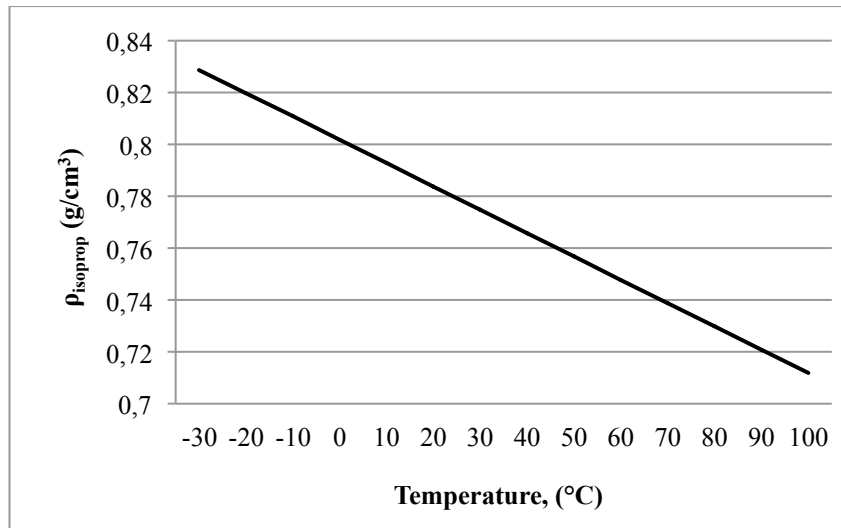
Figure 44 Density of isopropanol as function of temperature.

Appendix C

Images of porosity

Images from porosity analyses are presented below. The green areas were considered as pores.
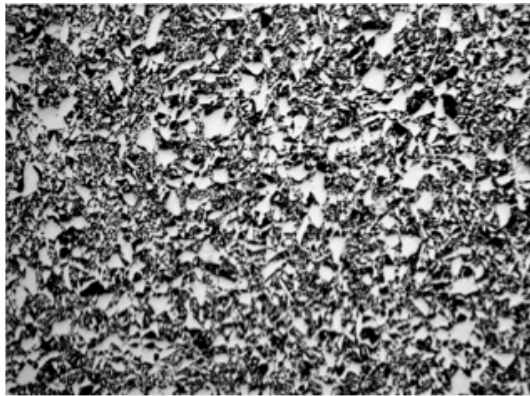
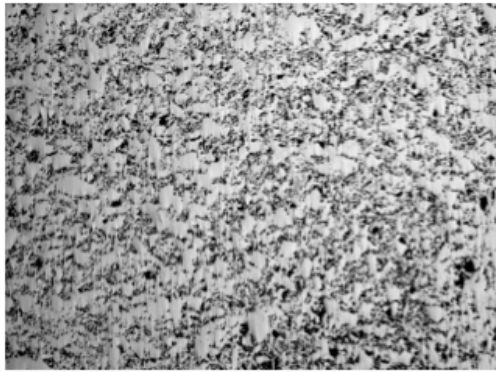a) 1300/30/30 inner part   400 μm
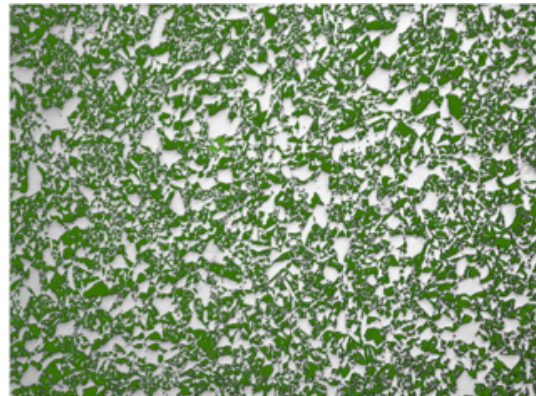
b) 1300/30/30 inner part (porosity)   400 μm
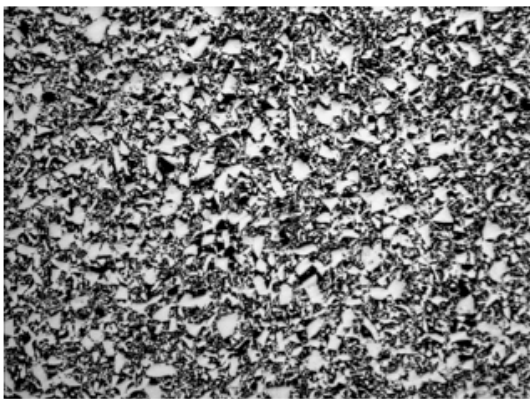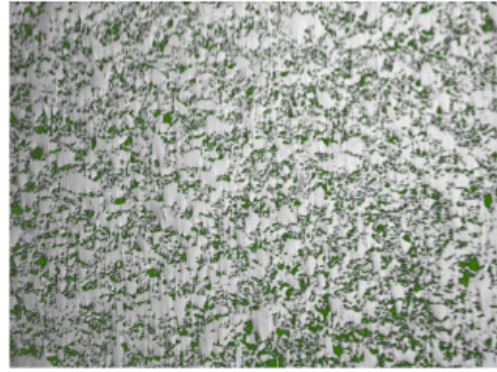
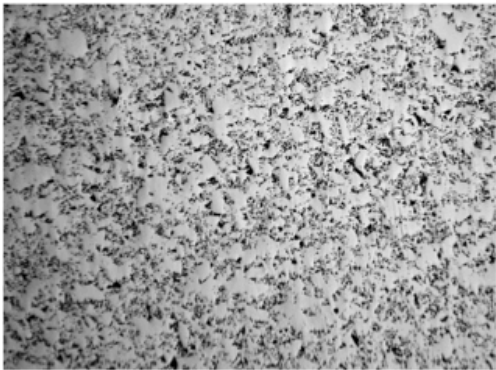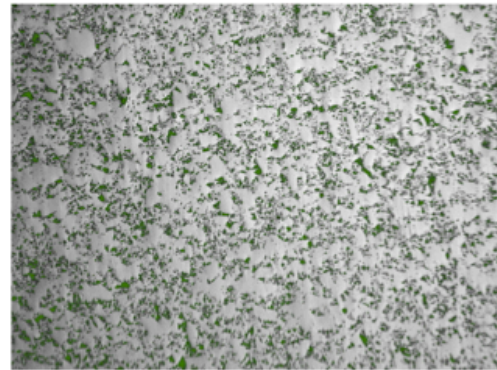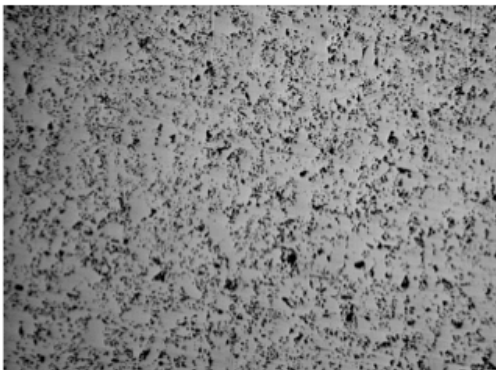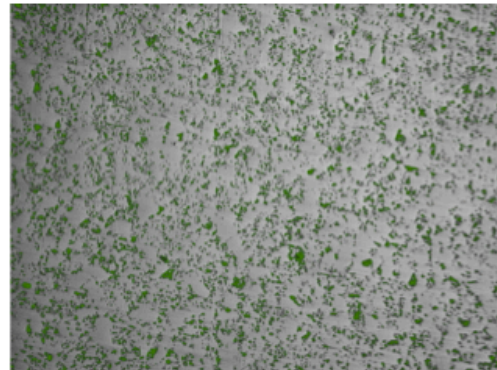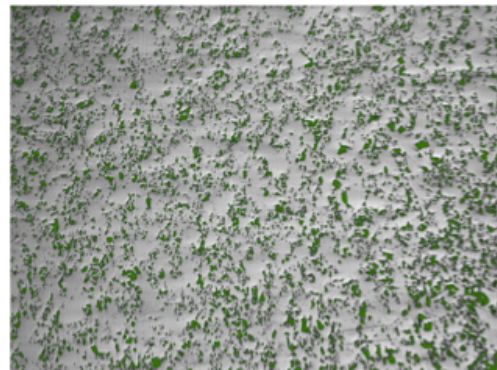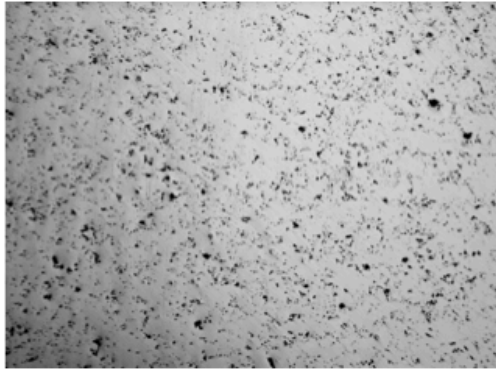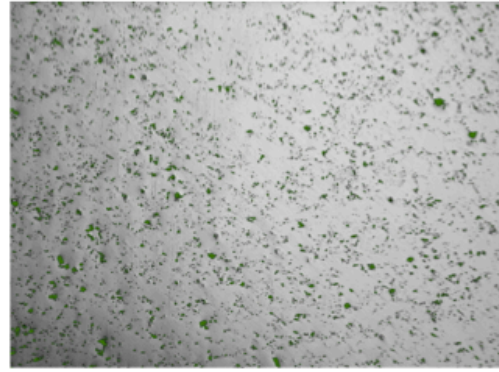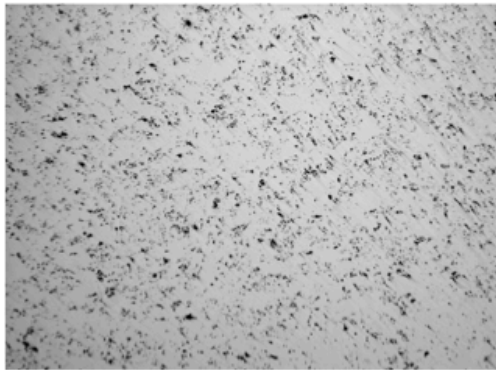c) 1300/30/30 outer part   400 μm
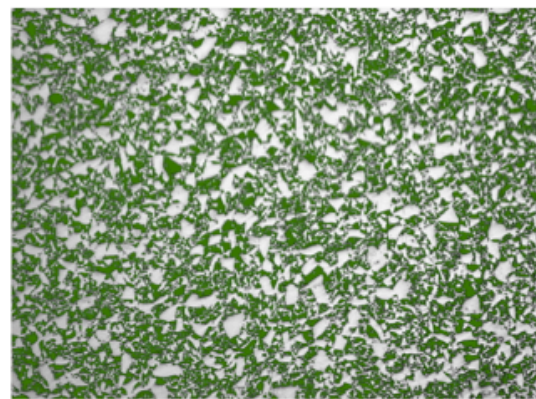
d) 1300/30/30 outer part (porosity)   400 μm
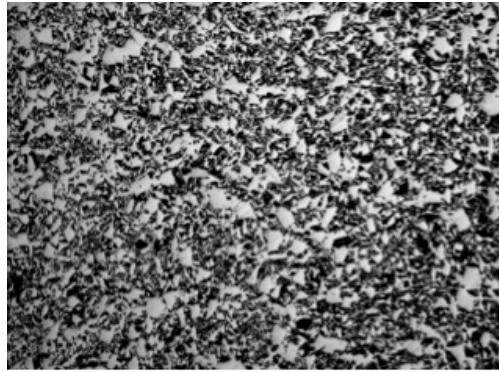
a) 1325/30/30 inner part   400 μm
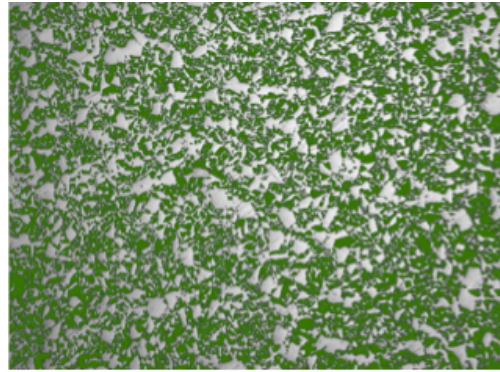
b) 1325/30/30 inner part (porosity)   400 μm
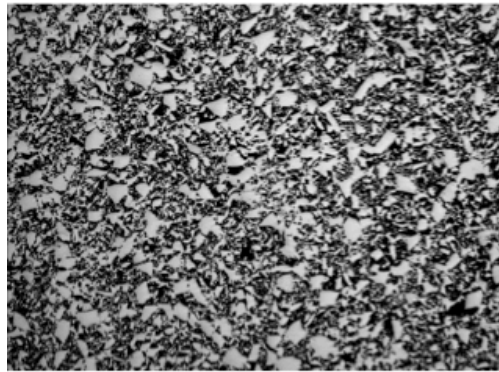
c) 1325/30/30 outer part   400 μm
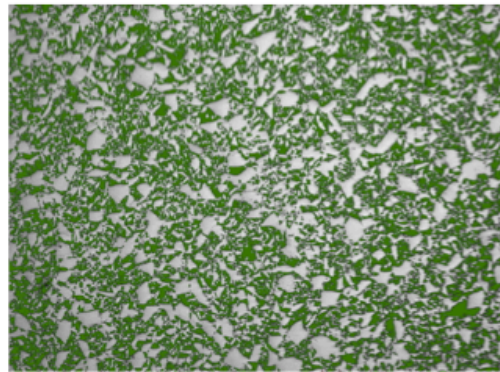
d) 1325/30/30 outer part (porosity)   400 μm
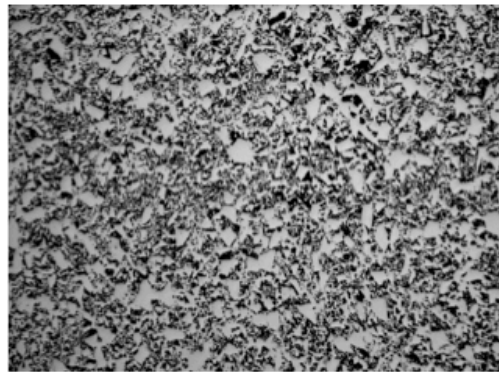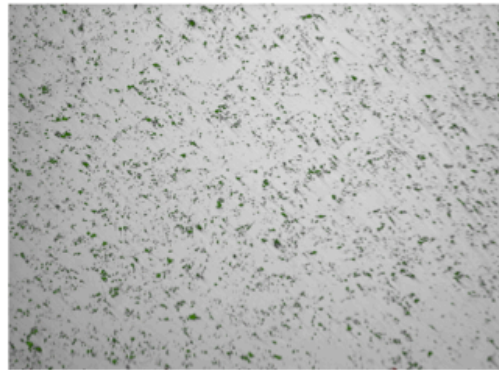

a) 1350/30/30 inner part   400 μm
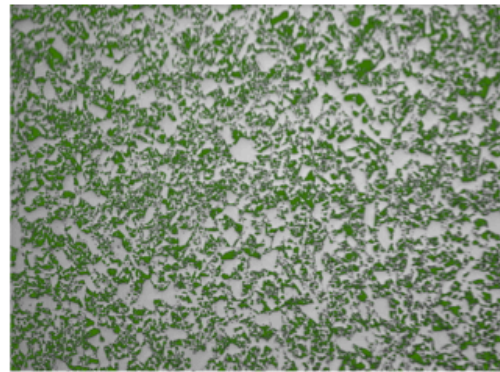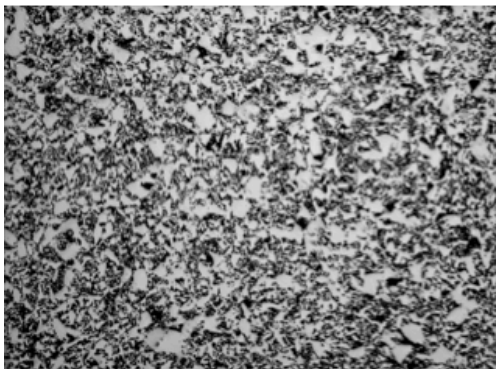

b) 1350/30/30 inner part (porosity)   400 μm
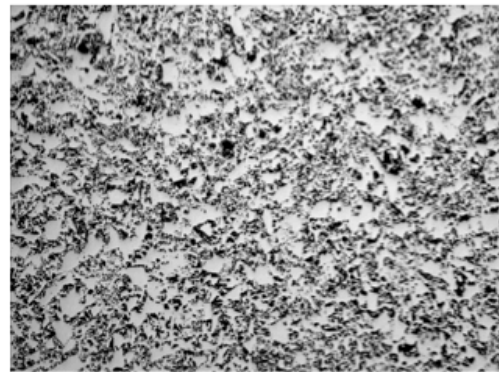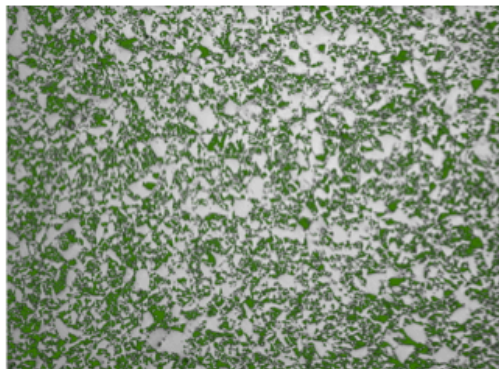

c) 1350/30/30 outer part   400 μm
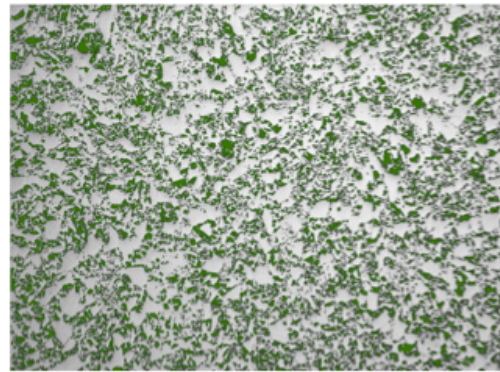
d) 1350/30/30 outer part (porosity)   400 μm

63
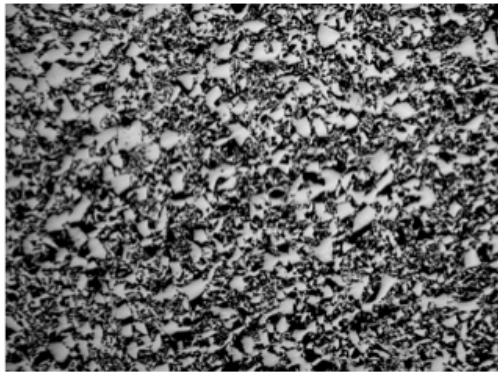
a) 1300/30/60 inner part   400 μm
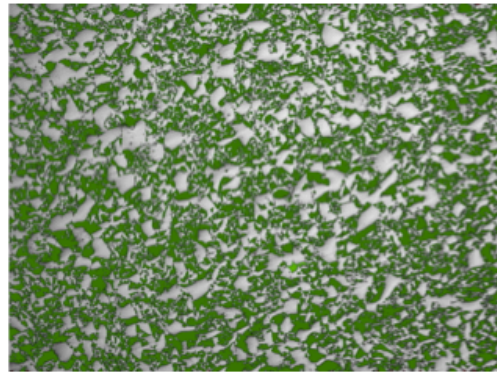
b) 1300/30/60 inner part (porosity)   400 μm
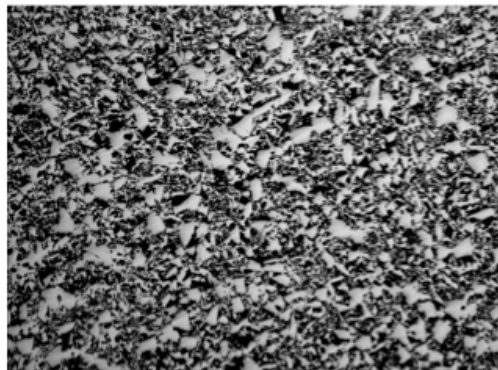
c) 1300/30/60 outer part   400 μm
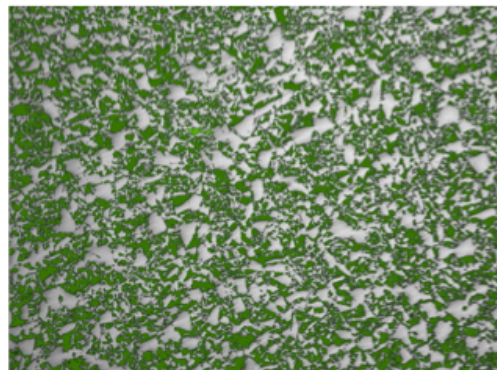
d) 1300/30/60 outer part (porosity)   400 μm
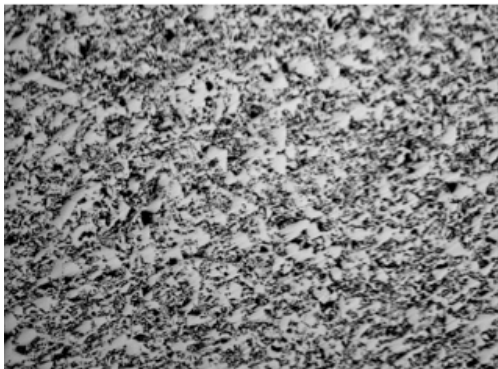
a) 1325/30/60 inner part   400 μm
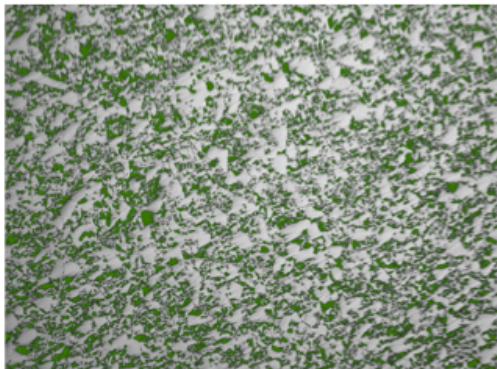
b) 1325/30/60 inner part (porosity)   400 μm
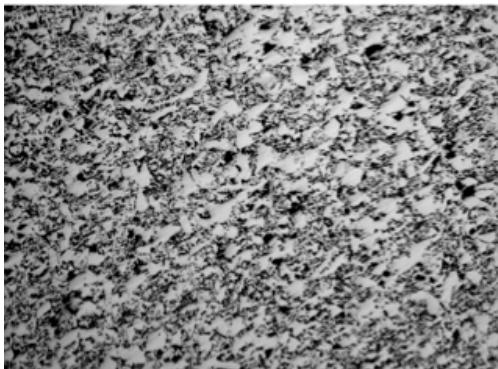
c) 1325/30/60 outer part   400 μm
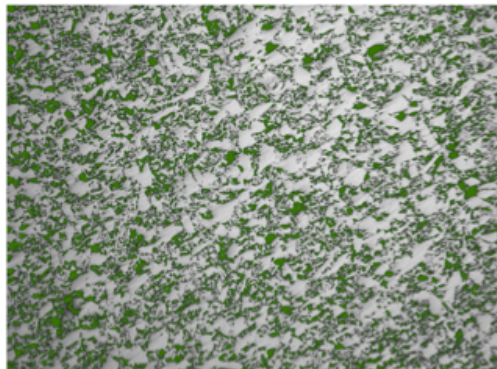
d) 1325/30/60 outer part (porosity)   400 μm
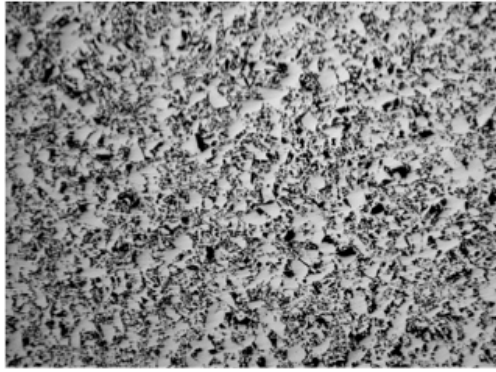
a) 1350/30/60 inner part   400 μm
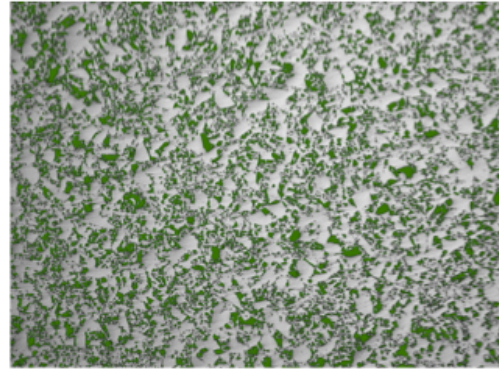
b) 1350/30/60 inner part (porosity)   400 μm
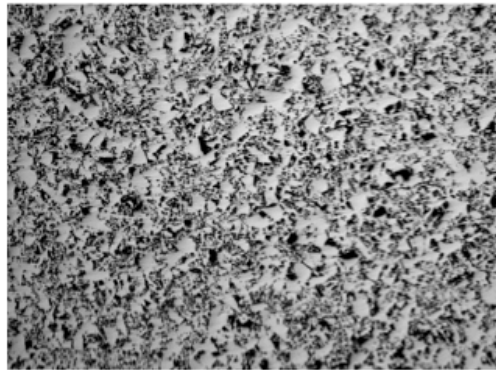
c) 1350/30/60 outer part   400 μm
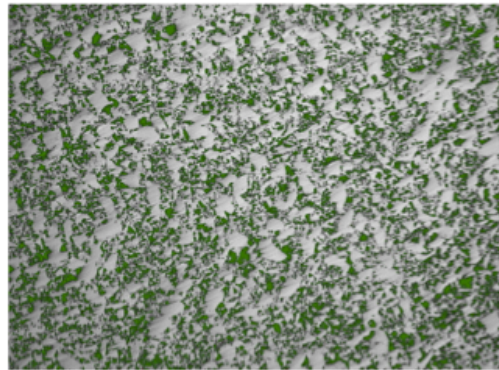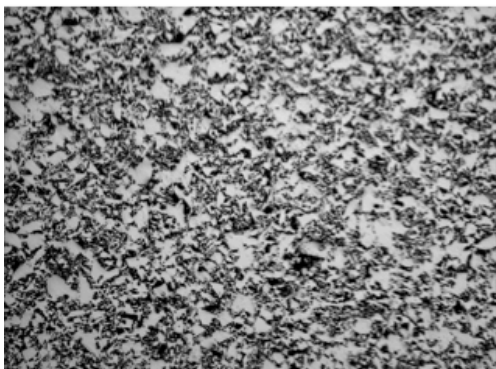

d) 1350/30/60 outer part (porosity)   400 μm
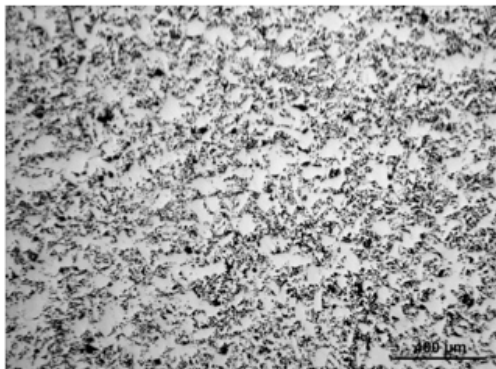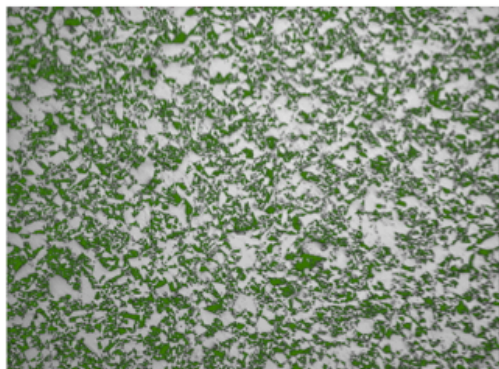

a) 1300/50/30 inner part   400 μm
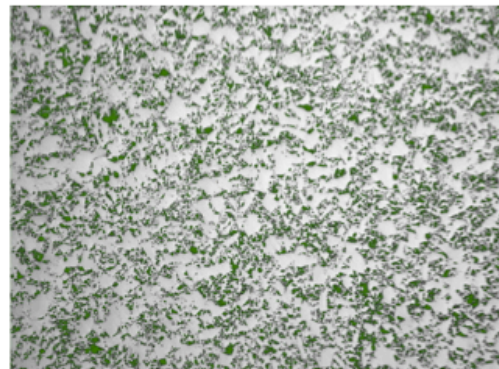
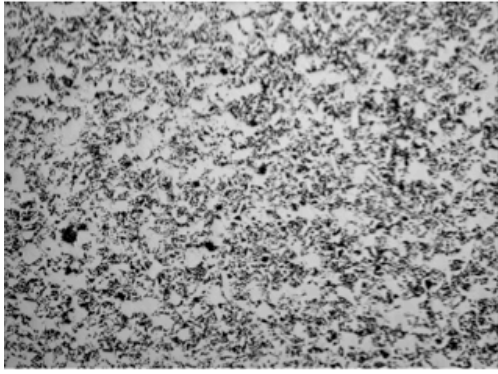b) 1300/50/30 inner part (porosity)   400 μm
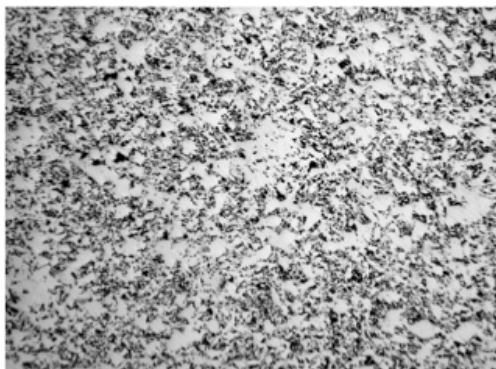
c) 1300/50/30 outer part   400 μm
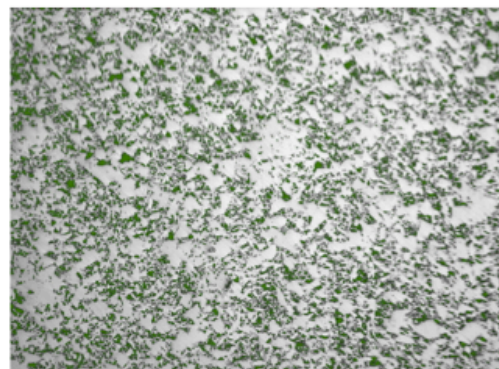
d) 1300/50/30 outer part (porosity)   400 μm

a) 1325/50/30 inner part   400 μm

b) 1325/50/30 inner part (porosity)   400 μm

c) 1325/50/30 outer part   400 μm

d) 1325/50/30 outer part (porosity)   400 μm

a) 1350/50/30 inner part   400 μm

b) 1350/50/30 inner part (porosity)   400 μm

c) 1350/50/30 outer part   400 μm

d) 1350/50/30 outer part (porosity)   400 μm

a) 1375/50/30 inner part   400 μm

b) 1375/50/30 inner part (porosity)   400 μm

c) 1375/50/30 outer part   400 μm

d) 1375/50/30 outer part (porosity)   400 μm

a) 1300/50/60 inner part   400 μm

b) 1300/50/60 inner part (porosity)   400 μm
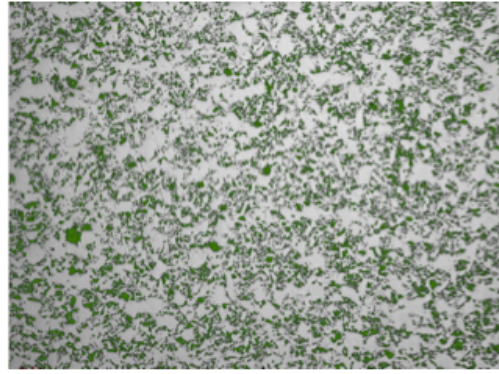
c) 1300/50/60 outer part   400 μm

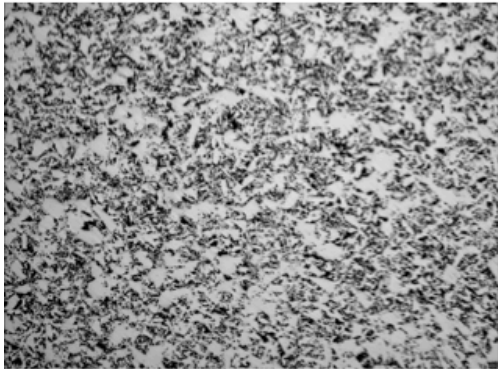d) 1300/50/60 outer part (porosity)   400 μm

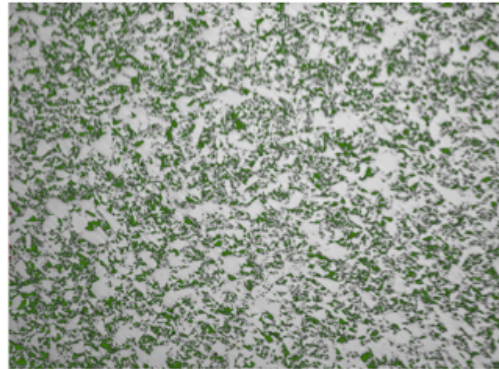a) 1325/50/60 inner part   400 μm

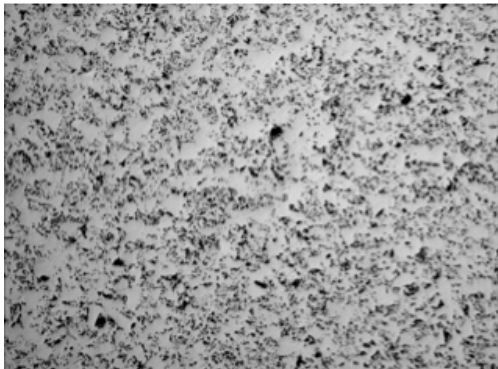b) 1325/50/60 inner part (porosity)   400 μm
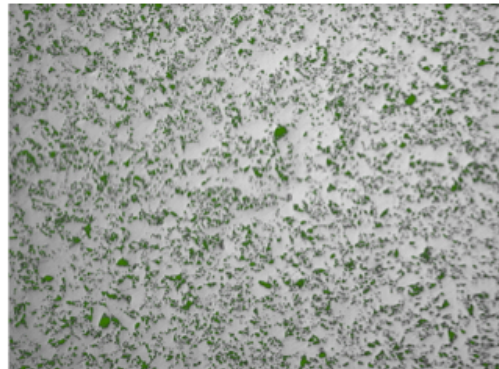
c) 1325/50/60 outer part   400 μm

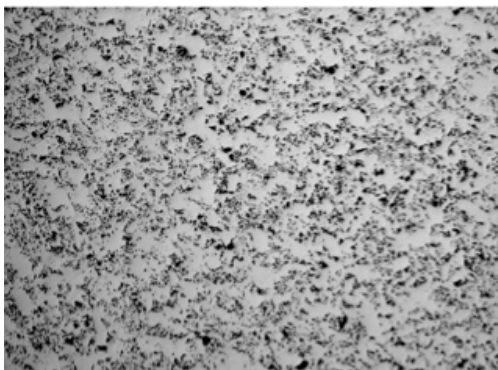d) 1325/50/60 outer part (porosity)   400 μm

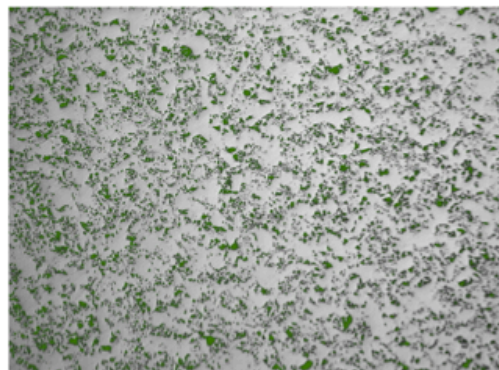a) 1350/50/60 inner part   400 μm

b) 1350/50/60 inner part (porosity)   400 μm

c) 1350/50/60 outer part   400 μm

d) 1350/50/60 outer part (porosity)   400 μm

Surface porosity and equivalent diameter are typed in Table 6. Purple background indicates samples that showed higher surface porosity in the outer edge compared to the inner part.

Table 6 Porosity data

Sample	Inner part Area fraction pores [%]	Inner part Equivalent diameter [µm]	Outer part Area fraction pores [%]	Outer part Equivalent diameter [µm]
1200/50/30	41,48	6,06	43,89	6,51
1300/50/30	7,95	3,93	7,92	3,82
1325/50/30	7,71	3,7	4,63	3,2
1350/50/30	6,24	3,88	7,51	3,98
1375/50/30	1,75	3,25	1,18	2,88
1300/30/30	27,98	7,18	26,07	7,06
1325/30/30	29,13	6,94	27,14	7,38
1350/30/30	17,92	5,58	13,45	4,91
1300/30/60	30,88	7,64	27,48	6,66
1325/30/60	14,66	5,04	13,43	4,61
1350/30/60	13,8	4,97	12,51	4,24
1300/50/60	17,41	5,28	16,57	5,3
1325/50/60	10,03	4,19	9,08	4,05
1350/50/60	5,28	3,51	5,78	3,71